

SOFIA FIFI-LS spectroscopy of DR21 Main: energetics of the spatially-resolved outflow from a high-mass protostar[★]

Agata Karska^{1,2,3}, M. Figueira^{1,4}, A. Mirocha⁵, M. Kaźmierczak-Barthel⁶, Ch. Fischer⁶, H. Wiesemeyer¹, I.-M. Skretas¹, A. Beck⁶, S. Khan¹, N. Lê⁷, Y.-L. Yang^{8,9}, L. Looney¹⁰, A. Krabbe⁶, F. Wyrowski¹, K. Menten¹

¹ Max-Planck-Institut für Radioastronomie, Auf dem Hügel 69, 53121, Bonn, Germany

² Argelander-Institut für Astronomie, Universität Bonn, Auf dem Hügel 71, 53121 Bonn, Germany

³ Institute of Astronomy, Faculty of Physics, Astronomy and Informatics, Nicolaus Copernicus University, Grudziądzka 5, 87-100 Toruń, Poland

⁴ National Centre for Nuclear Research, Pasteura 7, 02-093, Warszawa, Poland

⁵ Astronomical Observatory of the Jagiellonian University, Orla 171, 30-244 Kraków, Poland

⁶ Deutsches SOFIA Institut, University of Stuttgart, Pfaffenwaldring 29, 70569 Stuttgart, Germany

⁷ Institute For Interdisciplinary Research in Science and Education (IFIRSE), ICISE, 07 Science Avenue, Ghenh Rang Ward, 55121 Quy Nhon City, Binh Dinh Province, Vietnam

⁸ Star and Planet Formation Laboratory, RIKEN Cluster for Pioneering Research, Wako, Saitama 351-0198, Japan

⁹ National Radio Astronomy Observatory, 520 Edgemont Rd., Charlottesville, VA 22903 USA

¹⁰ Department of Astronomy, University of Illinois, 1002 West Green St, Urbana, IL 61801, USA

Received November 21, 2024; accepted March 17, 2025

ABSTRACT

Context. Massive star formation is associated with energetic processes that may influence the physics and chemistry of parental molecular clouds and impact galaxy evolution. The high-mass protostar DR21 Main in Cygnus X possesses one of the largest and most luminous outflows ever detected in the Galaxy, but the origin of its structure and driving mechanisms is still debated.

Aims. Our aim is to spatially resolve the far-infrared line emission from DR21 Main and to investigate the gas physical conditions, energetics, and current mass loss rates along its outflow.

Methods. Far-infrared SOFIA FIFI-LS spectra covering selected high- J CO lines, OH, [O I], [C II], and [O III] lines are analyzed across the almost full extent of the DR21 Main outflow using $2.00' \times 3.75'$ mosaic.

Results. The spatial extent of far-infrared emission follows closely the well-known outflow direction of DR21 Main in case of high- J CO, [O I] $63.18 \mu\text{m}$, and the OH line at $163.13 \mu\text{m}$. On the contrary, the emission from the [C II] $157.74 \mu\text{m}$ and [O I] $145.53 \mu\text{m}$ lines arises mostly from the eastern part of the outflow, and it is likely linked with a photodissociation region. Comparison of non-LTE radiative transfer models with the observed [O I] line ratios suggest H_2 densities of $\sim 10^5 \text{ cm}^{-3}$ in the western part of the outflow and $\sim 10^4 \text{ cm}^{-3}$ in the East. Such densities are consistent with the predictions of UV-irradiated non-dissociative shock models for the observed ratios of CO and [O I] along the DR21 Main outflow. Assuming that the bulk of emission arises in shocks, the outflow power of DR21 Main of $4.3 - 4.8 \times 10^2 L_\odot$ and the mass-loss rate of $3.3 - 3.7 \times 10^{-3} M_\odot \text{ yr}^{-1}$ are determined, consistent with estimates using $\text{HCO}^+ 1-0$.

Conclusions. Spatially-resolved far-infrared emission of DR21 Main provides a strong support for its origin in outflow shocks, and the stratification of physical conditions along the outflow. The total line cooling provides additional evidence that DR21 Main drives one of the most energetic outflows in the Milky Way.

Key words. stars:formation – stars: protostars – ISM: jets and outflows – HII regions – ISM: individual objects: DR21 Main

1. Introduction

High-mass stars have a powerful impact on the interstellar medium (ISM) of galaxies (Krumholz et al. 2014; Geen et al. 2020). Winds from massive stars efficiently shape their host molecular clouds, increasing the turbulence and dissipating some of their material (Luisi et al. 2021; Geen et al. 2021). During the evolved stages of high-mass star formation, H II regions form due to the emission of ionizing photons ($E \geq 13.6 \text{ eV}$), and they compress the surrounding molecular gas, triggering the formation of new generations of stars (Deharveng et al. 2005; Bernard et al. 2016). At the earliest stages of their formation,

deeply-embedded high-mass protostars drive energetic bipolar outflows (Bally 2016), which affect the physics and chemistry of their environments and the efficiency of star formation in clumps (Krumholz et al. 2014; Dale et al. 2015). Spatially-resolved observations are critical to assess the impact of outflows from such protostars onto their immediate surrounding and disentangle their multiple physical components.

Atomic and molecular tracers are useful probes of the physical conditions and energetic processes that occur in star forming regions. High- J ($J \geq 14$, $E_u/k_b \geq 580 \text{ K}$) rotational transitions of carbon monoxide (CO) are widely used to study the warm/hot gas components of outflows from deeply-embedded protostars (Herczeg et al. 2012; Manoj et al. 2013; Green et al. 2013; Karska et al. 2013, 2014b, 2018; Kristensen et al. 2017).

[★] This paper is dedicated to Karl Menten, our dear friend, mentor, and colleague, who first discovered the maser emission toward DR21 Main.

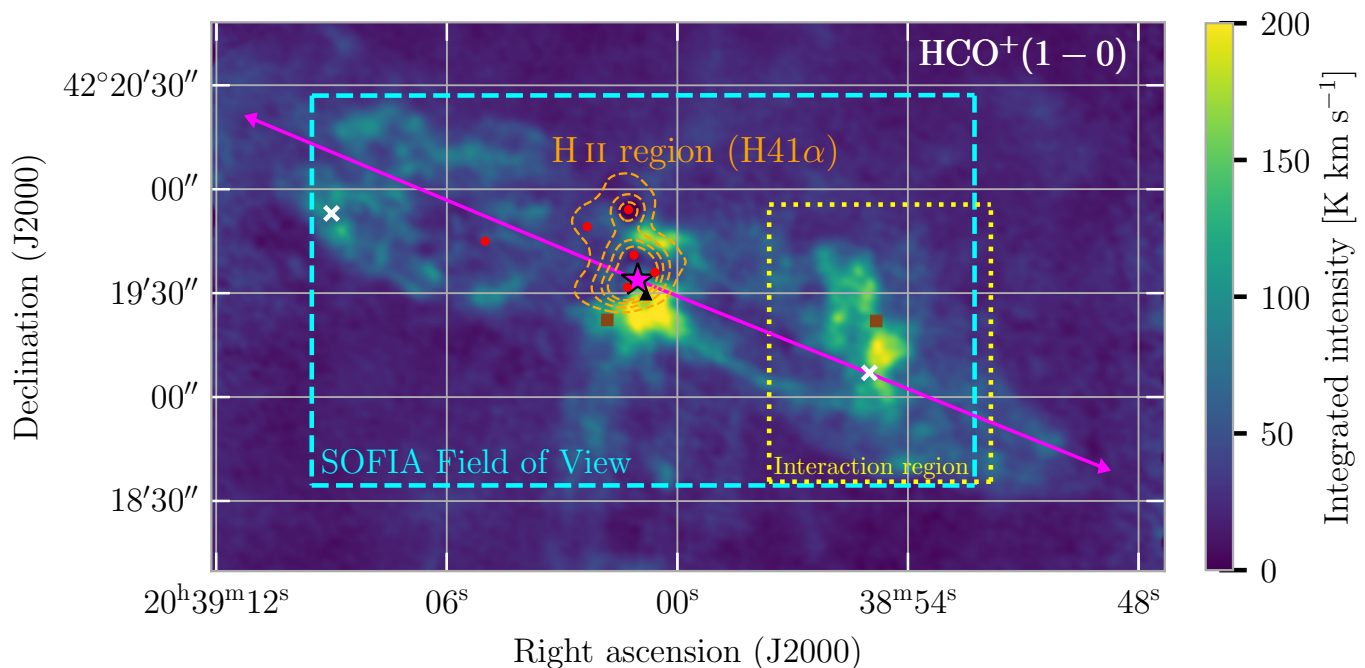


Fig. 1: Overview of the DR21 Main high-mass star-forming region. Overlay of the H41 α emission from DR21 integrated between -30 and 30 km s⁻¹ (orange dashed contours) on HCO⁺ 1-0 observations (colors) from IRAM 30 m and NOEMA (beam sizes of $2.60'' \times 2.36''$ and $3.29'' \times 2.74''$, respectively; Skretas et al. 2023). The yellow rectangle shows the interaction region (Skretas et al. 2023), and the light blue rectangle - the field-of-view of the FIFI-LS observations. The magenta star shows the center of the DR21-1 core at $(\alpha, \delta)_{J2000} = (20^h 39^m 01^s 03, +42^\circ 19' 33'' 8)$ following Cao et al. (2019) and the magenta arrows the outflow direction based on the HCO⁺ map (Skretas et al. 2023). The map also shows 6 positions of radio continuum sources identified as OB stars by Roelfsema et al. 1989 (red points), the 95 GHz methanol masers (brown squares) from Plambeck & Menten (1990), the 22 GHz H₂O maser (black triangle) from Genzel & Downes (1977), and the H₂ peaks (white \times symbols) (Garden et al. 1986).

Similar gas components are also evident in rotational lines of water (H₂O), originating mostly from shocks in the outflow cavity walls (Kristensen et al. 2012; Mottram et al. 2014, 2017). Additional important gas coolants of dense cores are fine-structure lines of [O I] and [C II], and mid-infrared (IR) lines of H₂ (Goldsmith & Langer 1978; Ceccarelli et al. 1996; Doty & Neufeld 1997), which are key diagnostic of photodissociation regions (PDRs, Tielens & Hollenbach 1985; Kaufman et al. 1999) and shocks (Kaufman & Neufeld 1996; Flower & Pineau Des Forêts 2010; Melnick & Kaufman 2015). These emission lines provide useful insight not only into the energetics of high-mass protostars, but also the characteristics of physical processes at play.

The *Herschel* Space Observatory (Pilbratt et al. 2010)¹ provided far-IR observations of several high-mass star formation sites consisting of deeply-embedded high-mass protostars (van Dishoeck et al. 2021) and more evolved H II regions (Motte et al. 2018). The high-resolution spectroscopy with the Heterodyne Instrument for the Far-Infrared on *Herschel* (HIFI, de Graauw et al. 2010) allowed the characterization of gas dynamics i.e., gas infall motions (Herpin et al. 2012, 2016; van der Tak et al. 2019), and outflows (van der Tak et al. 2013; San José-García et al. 2013, 2016). The Photodetector Array Camera and Spectrometer (PACS, Poglitsch et al. 2010) facilitated detections of all major gas cooling lines in the 50-200 μ m range, including high- J CO, H₂O, [O I], OH, and [C II] toward high-mass YSOs (Karska et al. 2014a; Oliveira et al. 2019; Cesaroni et al. 2023).

¹ *Herschel* is an ESA space observatory with science instruments provided by European-led Principal Investigator consortia and with important participation from NASA.

The spatial distribution of molecular line emission, however, was only analyzed toward a handful of high-mass protostars (Jacq et al. 2016; Leurini et al. 2017).

Subsequent observations with the Stratospheric Observatory for Infrared Astronomy (SOFIA; Young et al. 2012) provided additional velocity-resolved observations of outflow motions (Leurini et al. 2015; Hoang et al. 2023) and the spatial distribution of far-IR emission (Ossenkopf et al. 2015; Gusdorf et al. 2016; Schneider et al. 2018; Lê et al. 2023). The feedback of massive stars on their surrounding has been investigated using the large-scale maps of eleven high-mass star-forming regions in the [O I] and [C II] lines (Schneider et al. 2020; Tiwari et al. 2022; Beuther et al. 2022a; Bonne et al. 2022, 2023b), including the Cygnus X star-forming complex harboring low- and high-mass young stellar objects (YSOs) at different stages of their evolution (Schneider et al. 2006; Motte et al. 2007; Bontemps et al. 2010; Cao et al. 2019). The observations with the German REceiver for Astronomy at Terahertz frequencies (GREAT; Heyminck et al. 2012; Klein et al. 2012) revealed dynamic interactions of mostly atomic clouds in the DR21 and W75N star forming regions, leading to the formation of the high-density DR21 ridge (Bonne et al. 2023a; Schneider et al. 2023). The ridge hosts multiple star-forming clumps and cores, including one of the best-studied outflow source in the Milky Way, DR21 Main (Schneider et al. 2006, 2010; Beuther et al. 2022b; Skretas et al. 2023, Skretas et al., in preparation).

DR21 Main was a primary target of early IR space missions, due to the detection of its massive, highly collimated H₂ outflow (Garden et al. 1986, 1991). The outflow is located close to the

plane of the sky (see Figure 1) and has a linear scale of ~ 2.5 pc, adopting the distance of $1.5^{+0.08}_{-0.07}$ kpc from the measurements of trigonometric parallaxes (Rygl et al. 2012). The center of DR21 Main hosts two cometary H II regions associated with OB stars that could be responsible for the gas ionization (Harris 1973; Roelfsema et al. 1989; Cyganowski et al. 2003). Pathfinder far-IR observations with the NASA’s Kuiper Airborne Observatory (KAO) revealed extended emission in the [O I] line at $63.18 \mu\text{m}$, spatially-aligned with the $\text{H}_2 v = 1 - 0 \text{ S}(1)$ emission tracing shocked gas (Lane et al. 1990; Poglitsch et al. 1996). In addition, line emission from the [Si II] at $35 \mu\text{m}$ and [C II] line at $158 \mu\text{m}$ was detected in the central part of DR21 Main, pin-pointing the presence of a PDR (Lane et al. 1990). Subsequently, Jakob et al. (2007) measured the far-IR gas cooling using high- J CO lines ($J \geq 14$), [O I], [C I], and [C II] lines toward the central and two outflow positions of DR21 with the Long-Wavelength Spectrometer (Clegg et al. 1996) on board the Infrared Space Observatory (ISO, Kessler et al. 1996). Early *Herschel* observations with the Spectral and Photometric Imaging Receiver (SPIRE, Griffin et al. 2010) provided a full spectrum of DR21 Main from 194 to $671 \mu\text{m}$ including the first detection of H_2O , and several CO and ^{13}CO transitions within a single beam of $\sim 17 - 42''$ (White et al. 2010). Complementary spectroscopy with HIFI provided velocity-resolved profiles of selected H_2O , HCO^+ , and CO isotopologues, pin-pointing the contribution from both outflow shocks and PDRs to the far-IR emission from DR21 Main (Ossenkopf et al. 2010; van der Tak et al. 2010).

Complementary high angular resolution millimeter observations show a cluster of continuum sources at the center of DR21 Main (Skretas et al. 2023; Guzmán Ccolque et al. 2024). It supports the scenario that the bipolar outflow might be a product of the outflow alignment from multiple objects rather than being launched by a single driving source (Peters et al. 2014). The surrounding of DR21 Main shows indeed an exceptional outflow activity identified in near-IR H_2 emission (Davis et al. 2007; Smith et al. 2014). In addition, there is an observational evidence for the presence of an explosive event that occurred within the central region of DR21 Main (Zapata et al. 2013; Guzmán Ccolque et al. 2024). The fingerprints of the explosion (streamers) are perpendicular to the outflow direction and are likely unrelated to the bipolar outflow itself (Guzmán Ccolque et al. 2024), but nevertheless might affect the gas dynamics and excitation.

In this work, we aim to study the spatial distribution of far-IR line emission and its link with the main physical components of DR21 Main (outflow lobes, central H II regions). We also aim to determine the physical conditions of molecular, atomic, and ionized gas along the outflow, and discuss the likely origin of the far-IR emission. Finally, we aim to study the outflow energetics and its key properties such as outflow power and mass loss rates.

To this end, we present $2.00' \times 3.75'$ mosaics of DR21 Main covering its parsec-scale outflow from the SOFIA’s Field-Imaging Far-Infrared Line Spectrometer (FIFI-LS; Klein et al. 2014; Fischer et al. 2018). To account for the impact of unresolved absorption, we also use archival GREAT spectroscopy of [O I]. To complement the study of gas energetics, we also use the archival SPIRE maps of H_2O (Griffin et al. 2010).

The paper is organized as follows. Section 2 describes the observations and data reduction. Section 3 shows the emission spectra and maps of DR21 in far-IR. Section 4 contains the analysis of the gas excitation and calculation of the far-IR cooling budget. Section 5 discusses the origin of far-IR emission from DR21 Main and the energetics of the outflow, and Section 6 provides the conclusions.

2. Observations and data reduction

2.1. SOFIA FIFI-LS

Far-IR observations of DR21 were performed using the Field-Imaging Far-Infrared Line Spectrometer (FIFI-LS; Klein et al. 2014; Fischer et al. 2018) on the 2.5-m SOFIA telescope as part of the Guaranteed Time Observations (GTO) program (Project ID 87_0001, PI: R. Klein), Cycle 9 regular program (09_0079, PI: C. Fischer), and as part of the Directors Discretionary Time (DDT) program “Completing the FIFI-LS observations of DR21” (Project ID 75_0046, PI: R. Klein). The GTO program covered the [O I] lines at $63.18 \mu\text{m}$ and $145.53 \mu\text{m}$, and the [C II] line at $157.74 \mu\text{m}$. Complementary DDT observations targeted high- J CO lines, OH, and the [O III] line at $51.81 \mu\text{m}$, and Cycle 9 observations added the [O III] line at $88.35 \mu\text{m}$ and improved signal-to-noise in several previously observed lines (see Appendix A, Table A.1 for details).

FIFI-LS is an integral field unit (IFU) consisting of two grating spectrometers with a spectral coverage of $51\text{--}120 \mu\text{m}$ (blue) and $115\text{--}200 \mu\text{m}$ (red), facilitating simultaneous observations of selected wavelength intervals ($0.3\text{--}0.9 \mu\text{m}$ wide) in both channels (SOFIA Observer’s Handbook for Cycle 10²). The velocity resolution of ~ 150 (blue channel) to 600 km s^{-1} (red channel) provides unresolved spectral profiles. For comparison, *Herschel*/HIFI observations of $^{13}\text{CO } 10\text{--}9$ and $\text{H}_2\text{O } 1_{11} - 0_{00}$ toward DR21 Main show the line widths of a broad, outflow-related velocity components of ~ 15 and 24 km s^{-1} , respectively (van der Tak et al. 2010; Ossenkopf et al. 2010).

The FIFI-LS detector is composed of 5×5 spatial pixels (hereafter *spaxels*) and the same IFU design as the PACS spectrometer on *Herschel* (Poglitsch et al. 2010). The spaxel size is $6'' \times 6''$ in the blue channel (field-of-view, FOV, of $\sim 30''$) and $12'' \times 12''$ in the red channel (FOV of $\sim 1'$). Here, the on-the-fly (OTF) mapping mode was used in the cross directions to obtain a mosaic of 20 pointings in a symmetric chop mode. Each pointing covers $30''$ corresponding to the size of the field of view of the FIFI-LS blue array. The resulting maps are centered at $\text{RA}(J2000), \text{Dec}(2000) = 20^{\text{h}}39^{\text{m}}00^{\text{s}}.8, +42^{\circ}19'47''.7$.

The data were reduced using the FIFI-LS pipeline v.2.3.0 produced by the SOFIA Science Center, and the spectral cubes were corrected for the atmospheric absorption using ATRAN models (for the details of the method, see Fischer et al. 2021; Iserlohe et al. 2021). The idl-based software FLUXER v.2.78³ was used to produce the maps of continuum and line emission. The data was scaled with the spectral bin width. Subsequently, each map was convolved to the same angular resolution of $18.3''$, corresponding to the beamsize of the CO $14\text{--}13$ observations, and resampled to a pixel size of $2.4''$ with the same center and size using *Swarp* (Bertin et al. 2002).

The flux calibration accuracy of FIFI-LS is estimated as 10% (Fischer et al. 2018), and additional 10% uncertainty is assumed to account for the telluric effect, which most strongly affects the [O I] line at $63.18 \mu\text{m}$ (Sperling et al. 2021; Lê et al. 2023). The water vapor overburden for the [O I] line was determined between 5.9 and $3.5 \mu\text{m}$. With an error of 10% on this water vapor range, the transmission varies with flight parameters from 67% to 74% at $5.9 \mu\text{m}$, and from 77% to 82% at $3.5 \mu\text{m}$, both well within 10%.

Table 2 shows a comparison of the line fluxes obtained with SOFIA/FIFI-LS and ISO/LWS for the fine-structure lines at the

² <https://www-sofia.atlassian.net/wiki/spaces/OHFC1/overview>

³ <http://ciserlohe.de/fluxer/fluxer.html>

Table 1: Catalog of far-IR lines observed with FIFI-LS

Species	Transition	λ (μm)	E_u/k_B (K)	A_u (s^{-1})	g_u	θ ($''$)	1σ ($10^{-17} \text{ W m}^{-2}$)
CO	14-13	185.99	580.5	2.7(-4)	29	18.3	0.75
CO	16-15	162.81	751.7	4.1(-4)	33	16.1	0.27
OH	$3/2, 1/2-1/2, 1/2$	163.13	270.1	2.1(-2)	4	16.1	10.4
[O I]	$^3\text{P}_1-^3\text{P}_2$	63.18	227.7	8.7(-5)	3	7.1	1.95
[O I]	$^3\text{P}_0-^3\text{P}_1$	145.53	326.6	1.8(-5)	1	14.1	0.79
[C II]	$^2\text{P}_{3/2}-^2\text{P}_{1/2}$	157.74	91.2	2.3(-6)	4	15.6	2.15
[O III]	$^3\text{P}_2-^3\text{P}_1$	51.81	162.6	9.8(-5)	5	6.6	0.74
[O III]	$^3\text{P}_1-^3\text{P}_0$	88.35	162.81	2.7(-5)	3	9.2	0.36

Notes. Molecular data adopted from the Leiden Atomic and Molecular Database (LAMDA, Schöier et al. 2005) and the JPL database (Pickett et al. 1998). Data for [C II] and [O I] are obtained from Goldsmith et al. (2012) and Goldsmith (2019), and for [O III] from Moore (1985).

Table 2: Line fluxes from SOFIA and ISO toward the center of DR21 Main in units of $\text{erg cm}^{-2} \text{ s}^{-1} \text{ sr}^{-1}$

Line	λ	$F_\lambda(\text{FIFI-LS})$ (10^{-4})	$F_\lambda(\text{ISO})$ (10^{-4})	Difference
CO 14-13	185.99	2.68 ± 0.54	1.75	0.35
CO 16-15	162.81	2.89 ± 0.58	0.99	0.66
[O I]	63.17	73.27 ± 14.65	49.4	0.33
[O I]	145.53	8.08 ± 1.62	6.2	0.23
[C II]	157.74	15.05 ± 3.01	8.1	0.46
[O III]	51.81	11.70 ± 2.34	11.5	0.02
[O III]	88.35	10.15 ± 2.03	4.64	0.54

Notes. The ISO fluxes are adopted from Jakob et al. (2007) and refer to their position DR21 C. The SOFIA FIFI-LS fluxes are calculated within the ISO/LWS beam of $80''$. The difference is estimated as $1 - F_\lambda(\text{ISO})/F_\lambda(\text{FIFI-LS})$.

central position of DR21 Main over the region covered by the single ISO/LWS beam (Fig. 1). The relative difference is $\lesssim 50\%$ for the [C II] and [O I] $145.53 \mu\text{m}$ lines, and a few % for the [O I] line at $63.18 \mu\text{m}$. We conclude that the fluxes are in reasonable agreement given the flux uncertainties of LWS of $\sim 30\%$ (Jakob et al. 2007).

2.2. SOFIA GREAT

We reprocessed archival observations of DR21 Main from the German REceiver for Astronomy at Terahertz frequencies. GREAT was originally designed as a single-pixel, dual-color receiver (Heyminck et al. 2012) with high spectral resolution ($R \sim 2 \times 10^7$, Klein et al. 2012). Here we use data from its up-GREAT array (Risacher et al. 2018), which has seven pixels in a hexagonal layout and offers two frequency bands, tunable from 1.9 to 2.5 THz in the low-frequency array (LFA, with dual polarization), and in the high-frequency array (HFA, one polarization) to 4.7 THz (\pm several GHz, depending on the local oscillator configuration), allowing to cover the $63.18 \mu\text{m}$ fine-structure line of atomic oxygen, located on the wing of a broad telluric water vapor absorption feature.

The $^2\text{P}_{3/2}-^2\text{P}_{1/2}$ [C II] fine-structure line at 1900.5369 GHz has been obtained from observations executed in observatory cycle 7 (in December 2019 and March 2020), as part of the pro-

gram ID 07_0077 (P.I.: A.G.G.M. Tielens, N. Schneider). The $^3\text{P}_1-^3\text{P}_2$ [O I] line at 4744.77749 GHz was observed in June 2017, as part of the cycle 4 program ID 04_0111 (P.I.: E.T. Chambers). Beyond standard data reduction steps, we rejected spectra with bad baselines by analyzing the ratio of baseline noise to radiometric noise and masked spatially undersampled data at the map edges. We adopted beam efficiencies and widths calibrated on Mars by the instrument team. In the HFA, mixer gain drifts were mitigated by using the mesospheric [O I] line originating in the overlapping near-field beam patterns of the seven pixels. The original half-power beam widths are $14''1$ and $6''3$ (Risacher et al. 2018) in the LFA and HFA, respectively. For the [O I] $63.18 \mu\text{m}$ line, we then used a relatively wide convolution kernel for gridding, resulting in a final spatial resolution of $8''$ (HPBW) so as to better match the FIFI-LS beam.

3. Results

3.1. Spatial extent of the far-IR line emission

The spatial distribution of far-IR emission provides important insight into the physical components and processes responsible for the gas heating and cooling in the interstellar medium. The large extent of the DR21 Main outflow allows us to spatially resolve its substructures to study their far-IR line emission and identify physical processes that dominate the gas cooling.

Figure 2 shows the integrated intensity maps of DR21 Main in the CO 14 – 13 line at $185.99 \mu\text{m}$, the [O I] line at $63.18 \mu\text{m}$, and OH $3/2, 1/2-1/2, 1/2$ line at $163.13 \mu\text{m}$. The emission in all those tracers is clearly elongated in a similar fashion as the H_2 emission originating in outflow shocks (Garden et al. 1986, 1991; Davis et al. 2007). The peak of line emission is typically shifted with respect to the peak of the continuum emission at similar wavelengths. The far-IR continuum peaks, however, are consistent with the adopted coordinates of DR21 Main considering the beam size of FIFI-LS (see Fig. 2 and discussion in the Appendix A).

The emission in CO 14 – 13 shows rather discrete peaks of emission associated with the center of DR21 Main, and H_2 $v = 1 - 0 \text{ S}(1)$ peaks in the western and eastern outflow lobes (Garden et al. 1986). The CO 16 – 15 emission (Appendix A) extends more symmetrically over the entire mapped region. It shows a stronger emission peak in the western outflow lobe, characterized by the presence of dense gas (Plambeck & Menten 1990; Russell et al. 1992).

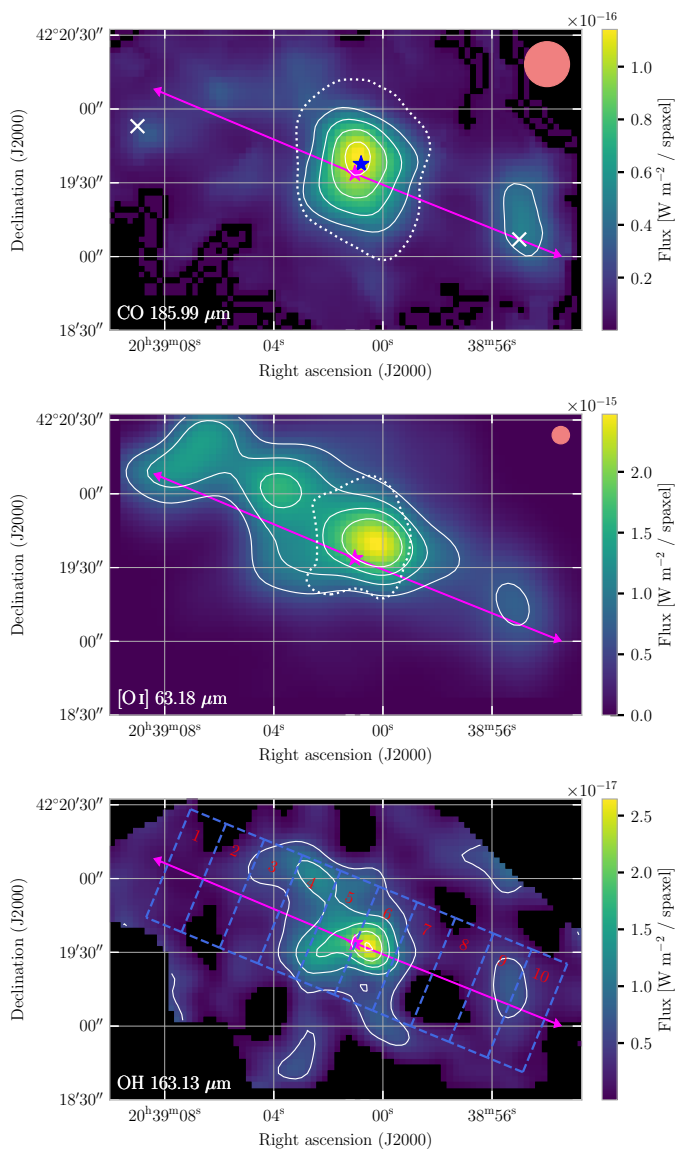


Fig. 2: Integrated intensity maps of the CO 14–13 line at 185.99 μm (top panel), the [O I] line at 63.18 μm (middle panel), and the OH line at 163.13 μm (bottom panel). Solid contours show the line emission in steps of 5σ , 8σ , 11σ , 14σ , 15σ (top panel), 35σ , 55σ , 75σ , 95σ (middle panel), and 5σ , 10σ , 15σ , 20σ , 25σ (bottom panel). Dotted contours show the extent of the continuum emission at the 5σ level. The magenta and blue stars show the DR21-1 core (Cao et al. 2019) and the center of the explosive outflow at $(\alpha, \delta)_{J2000} = (20^{\text{h}}39^{\text{m}}00^{\text{s}}.8, +42^{\circ}19'37''.62)$ from Guzmán Ccolque et al. (2024)

, magenta arrows the outflow direction from HCO^+ (Skretas et al. 2023) and white \times symbols the H_2 peaks (Garden et al. 1986). The maps were convolved with the beam size at 186 μm , represented by the orange circle at the map. For a comparison, the original beam size at 63 μm is also shown. The blue dashed grid lines show the area of ten boxes used for the analysis of the far-IR emission along the outflow direction (see Section 3).

The [O I] 63.18 μm emission is elongated across the full extent of the DR21 Main outflow (Fig. 2). The area of the emission is similar to earlier maps obtained with KAO (Poglitsch et al. 1996) and ISO (Lane et al. 1990), but the level of detail is significantly higher due to the improvement in the spatial resolution (a

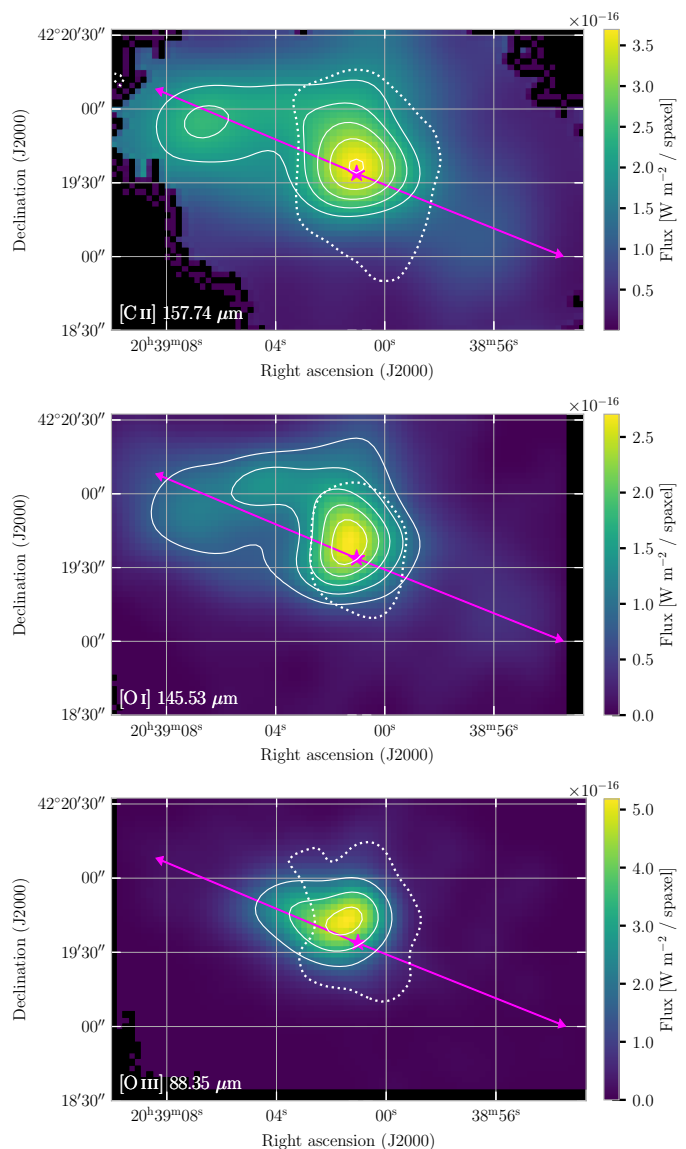


Fig. 3: Integrated intensity maps of the [C II] line at 157.74 μm (upper panel), [O I] line at 145.53 μm (middle panel), and [O III] line at 88.35 μm (bottom panel). Solid contours show the steps of 9σ , 11σ , 13σ , 15σ , 17σ (upper panel), 10σ , 15σ , 20σ , 25σ , 30σ (middle panel), and 10σ , 30σ , 50σ , 70σ (bottom panel). Dotted contours show the extent of the continuum emission in the close vicinity of the targeted lines at the 5σ level.

factor of 5 between ISO/LWS and SOFIA/FIFI-LS). In particular, this allows us to notice a spatial shift between the peaks of the [O I] and CO 14-13 emission in the vicinity of DR21 center (Fig. 2). Moreover, there is a systematic shift of the [O I] emission to the North from the outflow direction in the eastern outflow lobe, which is drawn based on the HCO^+ 1-0 maps (see Fig. 4, Skretas et al. 2023). This is most likely due to the differences in the excitation conditions for the [O I] and CO 14-13 lines, and the fact that some [O I] likely arises also in a central PDR.

The pattern of OH 163.13 μm emission is significantly more compact than those of high- J CO and [O I] lines (Fig. 2). Nevertheless, it shows an elongated pattern extending from North-East to South-West, and a clear emission peak at the western lobe where peaks of H_2 , CO, and [O I] are also detected. This suggest a similar, outflow-related origin of OH emission, as also

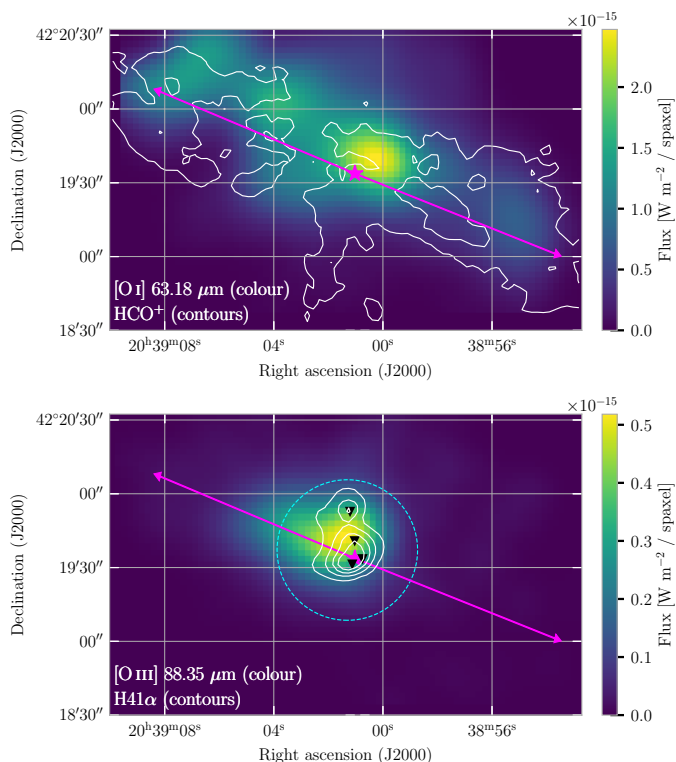


Fig. 4: Integrated intensity maps of the the [O I] line at $63.18 \mu\text{m}$ with HCO^+ 1-0 in solid contours at 5σ (upper panel), and [O III] line at $88.35 \mu\text{m}$ with $\text{H41}\alpha$ in solid contours with steps of 5σ , 20σ , 40σ , 60σ (lower panel). The cyan dashed circle represents the H II region identified in the Global view on Star formation in the Milky Way (GLOSTAR; Brunthaler et al. 2021) survey (Khan et al. 2024), and the black downward triangles show the cometary sources observed for the first time by Harris (1973).

suggested for other low- and high-mass protostars observed with *Herschel* (Wampfler et al. 2011, 2013; Karska et al. 2014b), SOFIA (Laurini et al. 2015), and *James Webb Space Telescope* (Caratti o Garatti et al. 2024; Neufeld et al. 2024; Tychoniec et al. 2024; van Gelder et al. 2024). Some weaker emission extends also to the South, along the dense material in the DR21 ridge, which is only seen in this tracer. Noteworthy, this is the first detection of OH in emission towards DR21 Main; the *Herschel*/PACS observations of the ground-state OH $119 \mu\text{m}$ line and the continuum toward the center of DR21 Main show strong absorption at low spectral resolution and will not be included in our analysis.

Figure 3 shows the integrated intensity maps of DR21 Main in the [C II] line at $157.74 \mu\text{m}$, the [O I] line at $145.53 \mu\text{m}$, and the [O III] line at $88.35 \mu\text{m}$. The bulk of emission in those species is located in the eastern outflow-lobe and is absent from the western outflow lobe. Noteworthy, the emission is elongated along the H_2 outflow direction for all atomic and ionic species, but most compact for [O III]. The patterns of the [C II] and [O I] $145.53 \mu\text{m}$ emission strongly resemble each other, but differ from the [O I] $63.18 \mu\text{m}$ line extending toward the western outflow lobe (Fig. 3). Possible reasons behind those differences will be discussed in Section 3.2.

Figure 4 compares the observations from FIFI-LS to those recently obtained by Skretas et al. (2023) as part of the Cygnus Allscale Survey of Chemistry and Dynamical Environments (CASCADE; Beuther et al. 2022b), a Max-Planck-IRAM Ob-

serving Program on NOEMA and IRAM-30 m. The [O I] $63.18 \mu\text{m}$ emission resembles the HCO^+ 1-0 emission interpreted as an outflow tracer in DR21 Main (Skretas et al. 2023). This is particularly the case in the western outflow lobe, where the region of enhanced emission in [O I] and HCO^+ coincides with the H_2 emission peak and the so-called “interaction region” (Skretas et al. 2023). In the eastern lobe, however, the [O I] $63.18 \mu\text{m}$ emission seems to trace only the northern part of the outflow seen in HCO^+ ; it is also detected in the cavity of molecular gas located midway between the center of DR21 Main and the H_2 peak (see also the *Spitzer*/IRAC image of Zapata et al. 2013).

The cavity region also consists of the [O III]-emitting, ionized gas, which seems to be linked with two well-studied H II regions at the center of DR21 Main (Harris 1973; Roelfsema et al. 1989; Cyganowski et al. 2003). The part of [O III] emission that extends beyond the $\text{H41}\alpha$ emission in the outflow direction (Fig. 4) spatially coincides with the 6 cm continuum emission, which traces a southern, cometary H II region (Cyganowski et al. 2003). A similar, elongated pattern of emission is also seen in the [N II] $^3\text{P}_1-^3\text{P}_0$ line at $205.2 \mu\text{m}$ with *Herschel*/SPIRE (White et al. 2010).

FIFI-LS maps illustrate the complexity of far-IR emission arising from the DR21 Main outflow as it interacts with the surrounding medium. The observations show an asymmetry between the atomic/ionic and molecular line emission, which suggest different excitation conditions along the outflow. The spatial differences in far-IR emission will be further investigated as a function of the offset from the DR21 center in Sections 3.2 and 4.1.

3.2. Emission spectra

FIFI-LS spectroscopy reveals bright far-IR emission arising from molecular, atomic, and ionized gas components, illustrating a range of physical conditions along the DR21 Main outflow.

To study the line emission in various species, we integrated their emission inside ten boxes along the outflow major axis, separately for each species (Fig. 2). We chose the area for integration to ensure a continuous coverage of emission on the maps (see Appendix C).

The line fluxes are calculated inside each box of $0.12 \times 0.36 \text{ pc}^2$ assuming a distance of 1.5 kpc (Rygl et al. 2012). To calculate the uncertainties, we first estimate the noise as the standard deviation of the continuum part of the spectrum. This noise is added to the spectrum, and a Gaussian fitting is performed. This process is repeated for each pixel 500 times. The uncertainty is estimated as the standard deviation of the Gaussian’s peak intensities, to which we add 20% of the flux to obtain the total uncertainty on the flux.

Figure 5 shows a line inventory in all transitions targeted by FIFI-LS along the DR21 Main outflow (Table 1). The [O I] line at $63.18 \mu\text{m}$ and the [C II] line at $157.74 \mu\text{m}$ are the strongest observed far-IR lines. The CO 14 – 13 line at $186.0 \mu\text{m}$ and the CO 16 – 15 line at $162.81 \mu\text{m}$ are detected in all boxes, whereas the [O III] transitions at 51.81 and $88.35 \mu\text{m}$ are firmly detected only in the eastern outflow lobe (boxes 1-6).

All lines observed with FIFI-LS are velocity-unresolved, and any shifts in velocity are instrumental (Fig. 5). In reality, several effects might affect the line profiles and fluxes of those spectra including line optical depths, absorption due to foreground gas, or imperfect telluric correction (Section 2.1). The self-absorption is expected to affect primarily the [O I] $63.18 \mu\text{m}$ line, since oxygen is typically most populated in the ground level (Nisini et al. 2015). In fact, early observations with KAO performed with a

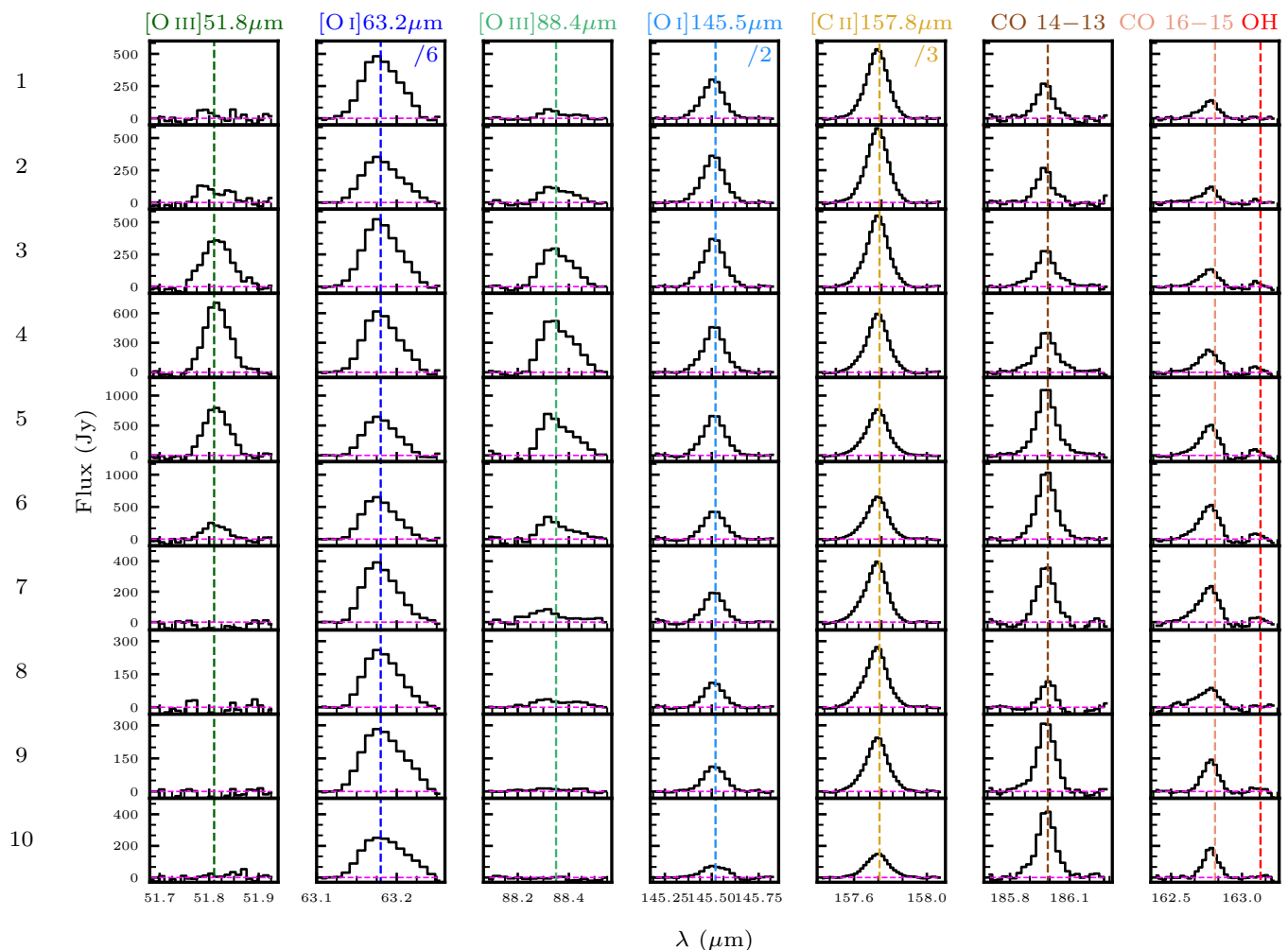


Fig. 5: Continuum-subtracted FIFI-LS spectra of far-IR emission lines detected toward DR21 Main (see Table 2). Each row corresponds to the emission integrated in the boxes of $16.5'' \times 50''$ each along the DR21 Main outflow, with position numbers increasing from East to West (see Appendix C, Fig. C.1, and also Fig. 2). The spectra of [O I] 63.18 μm , [O I] 145.53 μm , and [C II] 157.74 μm are divided by factors of 6, 2, and 3, respectively.

velocity resolution of 7 km s^{-1} revealed a significant drop of [O I] emission around 10 km s^{-1} , and interpreted as the foreground material associated with W75 (Poglitsch et al. 1996). In the 145.53 μm [O I] line, the FIFI-LS spectra may also suffer from an incorrectly removed telluric ozone feature.

To test the impact of absorption on the FIFI-LS line fluxes, we analyze the archival observations from SOFIA/GREAT covering several boxes along the DR21 Main outflow (Figure 6; Appendix B). Absorption is most evident in velocity range from -15 to 10 km s^{-1} , so likely arise both at source velocity of -3 km s^{-1} as well as at the velocity of the W75 complex (Dickel et al. 1978). For each of the boxes, we mask the part of the profile affected by absorption and fit a Gaussian profile to the line wings. We calculate the ratio of the flux from the Gaussian fit and flux integrated over the observed line profile, a so-called correction factor, to estimate the amount of “missing flux” due to absorptions. Subsequently, we use the correction to multiply the flux measured with FIFI-LS, where the absorptions are fully unresolved, to recover the total flux within each of the boxes.

Appendix B shows the results of this analysis for the [O I] 63.18 μm line. We find that the FIFI-LS fluxes in this line are underestimated by a factor of 1.76 ± 0.16 (a range from 1.5 to

2.0 in 4 boxes), which affects the spatial distribution of the line emission and the line ratios when considering only FIFI-LS measurements.

A similar analysis could not be performed for the 145.53 μm line due to strong line blending with atmospheric ozone. The analysis of the [C II] line profiles, showing additional velocity components than [O I], is beyond the scope of this paper and will be presented in Ossenkopf et al. (in preparation). In the subsequent analysis, we implement the correction for the [O I] 63.18 μm and discuss its impact on the final results.

In summary, far-IR lines are firmly detected toward DR21 Main, pin-pointing regions of intensive molecular, atomic, or ionic gas cooling. The impact of unresolved absorption has been quantified for the [O I] 63.18 μm and [C II] lines using high spectral resolution observations from GREAT.

4. Analysis

Spatially-resolved emission in various molecular and atomic species can help to understand the physical processes responsible for gas cooling in the far-IR regime. The analysis of line luminosities, combined with radiative transfer models, provides

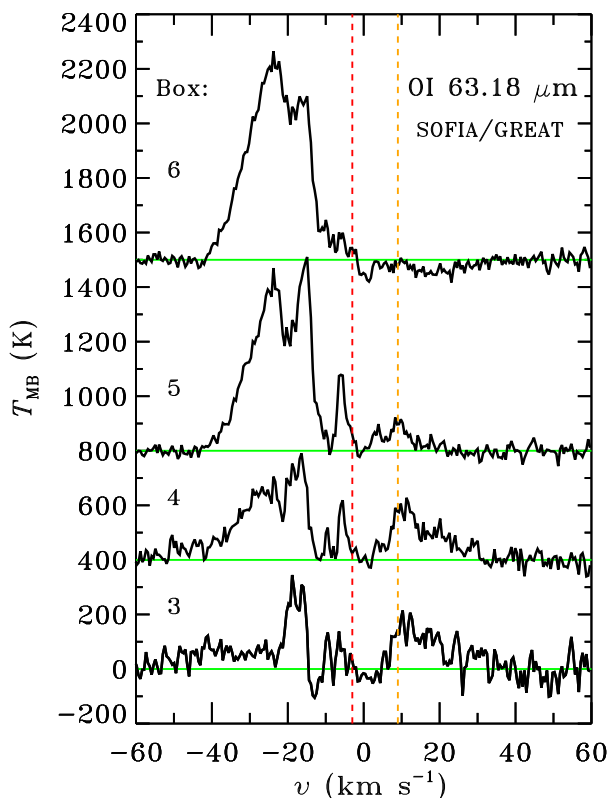


Fig. 6: Line profiles of the [O I] 63.18 μm in boxes 3, 4, 5, and 6 from SOFIA/GREAT. The y-axis offsets are used to improve the clarity of the figure. Vertical lines correspond to the source velocity (in red) and the velocity of foreground material from W75 complex (in orange, Dickel et al. 1978).

constraints on physical conditions of the species observed with FIFI-LS along the DR21 Main outflow major axis.

4.1. Far-IR line luminosities

Far-IR maps of DR21 Main show different patterns in molecular versus atomic/ionic lines, as well as some asymmetries between the eastern and western outflow-lobes (Section 3.1). Here, we examine how the emission in each species changes as a function of position along the DR21 Main outflow.

Figure 7 shows the line luminosity of each species as a function of the distance from the center of DR21 Main. The highest luminosities are associated with the central position in all lines. The [O I] 63.18 μm line, as well as CO 16-15 and OH lines, show an almost equally strong luminosity at +7.5'' and -8.1'' offset. Their emission clearly extends towards the western outflow lobe associated with the interaction region (offsets from -55 to -70''; Section 3.1). However, the eastern outflow lobe shows a significantly larger luminosity of [O I] 63.18 μm , similar to [C II] (Fig. 7). The ratio of the [O I] 63.18 μm line luminosity between offsets +39'' and -39'' of ~ 2.3 is slightly higher than for the ratio of [C II] emission in the same offsets (the ratio of ~ 2.0 ; see Appendix C), and shows a plateau in the eastern outflow lobe. Such excess emission is consistent with early measurements with the KAO covering offsets up to $\pm 140''$ (Lane et al. 1990). [O I] emission measured by the KAO decreases beyond the offset of -80'' in

the western lobe, not covered by our FIFI-LS observations (Fig. 7).

Line luminosities of the [C II] and [O I] 145.53 μm lines follow a similar pattern along the DR21 Main outflow, and show a clear excess luminosity in the eastern outflow lobe (Fig. 7, see also Section 3.1). Noteworthy, the decrease of luminosity from the center to the outflow-lobes is steeper in the [O I] 145.53 μm line; for instance, the ratio of the line luminosity between the center and the offset -39'' is ~ 6.3 and ~ 2.8 for the [O I] and [C II] lines, respectively (Appendix C). As a result, [C II] emission is more strongly associated with the outflow lobes; it extends to the offset of -120'' according to KAO observations, similar to the [O I] 63.18 μm line (Lane et al. 1990).

Finally, the [O III] lines at 51.81 and 88.35 μm peak at the center of DR21 Main and at the offset of +23'', corresponding to the cometary H II regions (Fig. 3) and the atomic/ionic gas cavity in the eastern outflow lobe (Section 3.1). Both luminosity patterns show a similar, asymmetric shape, characterized by a steep decrease of luminosity in the western outflow-lobe, similar to the pattern in [Si II] line from the KAO (Lane et al. 1990). Noteworthy, the 51.81 μm line shows a discrete peak of emission in the interaction region, but a lack of detections in intermediate offsets, which might suggest a local production of ionizing photons in the interaction region (see also Appendix A).

In the following sections, we will investigate the physical conditions behind the far-IR line luminosities across the outflow. The ratios of pairs of CO, [O I], and [O III] lines will provide key insight into the gas excitation in various physical components of DR21 Main.

4.2. Physical conditions

Large-scale mapping of several transitions of the same species allows us to determine temperature profiles along the major axis of the DR21 Main outflow. We determine physical conditions of the molecular, atomic, and ionized gas components, and compare them to previous low angular-resolution studies. Firstly, we consider a simplified case of gas in Local Thermodynamic Equilibrium, LTE. Secondly, we perform radiative-transfer models accounting for non-LTE excitation and line optical depths.

4.2.1. Molecular gas component

FIFI-LS observations allow the calculation of the CO excitation temperature using two high- J CO transitions: 14-13 and 16-15. Assuming LTE conditions and using molecular line data from Table 1, $T_{\text{exc}}^{\text{CO}}$ can be expressed as (see, e.g. Jakob et al. 2007):

$$T_{\text{exc}}^{\text{CO}} = 171.2 \times \ln^{-1}(1.974 \times R_{\text{CO}}), \quad \text{for } R_{\text{CO}} > 0.51 \quad (1)$$

where R_{CO} refers to the luminosity ratio of the CO 14-13 and CO 16-15 lines. The observed ratios of the CO lines range from ~ 0.8 -1.4 (Table 3), all in excess of 0.5, so Eq. 1 can be used to derive the CO excitation temperatures along the DR21 Main outflow. The resulting temperatures range from 166 ± 32 K to 360 ± 160 K, with a median of 240 K. The highest temperatures, in excess of 300 K, are measured in Boxes 4, 6 and 7, coinciding with the emission peaks of [O I] 63.18 μm line (Fig. 2).

The distribution of CO excitation temperatures might be influenced by differences in gas densities along the DR21 Main outflow. In particular, for H₂ densities below the critical densities of the observed CO lines, $n_{\text{crit}}^{\text{CO}} \sim 2.7 - 3.7 \times 10^6 \text{ cm}^{-3}$ at 300 K (Schöier et al. 2005), the LTE assumption might not be justified. Therefore, we calculate non-LTE radiative-transfer models

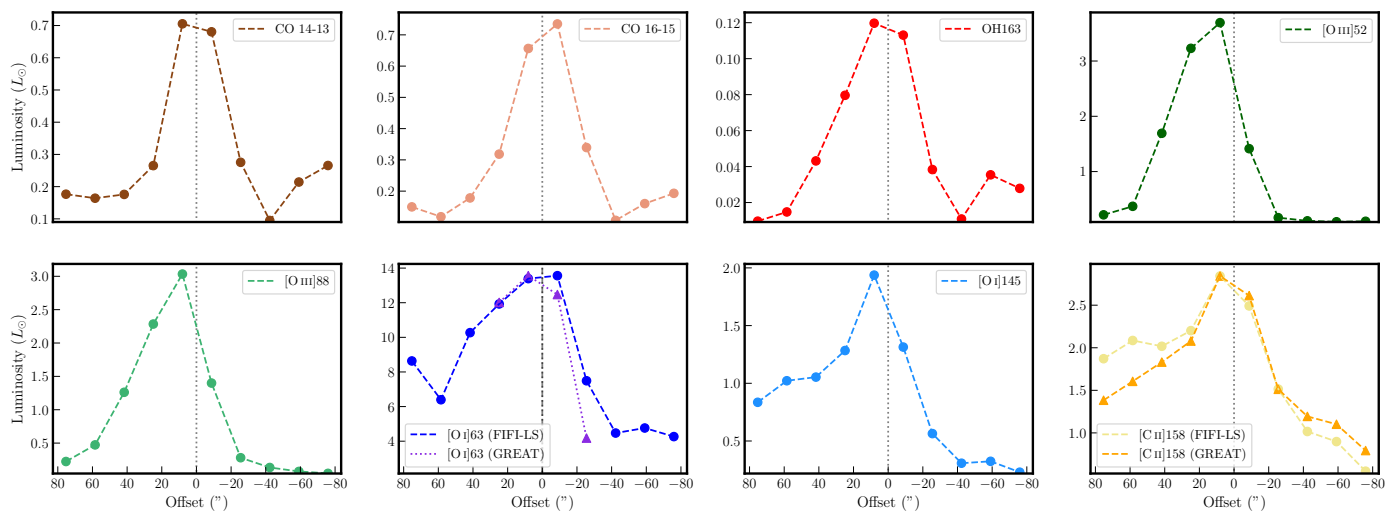


Fig. 7: Luminosities of far-IR lines observed with FIFI-LS (dashed-lines) and GREAT (dotted-lines) along the major axis of the DR21 Main H_2 outflow, integrated inside 10 boxes of $16.5'' \times 50''$ each (the same boxes as in Fig. 5). The luminosities for [O I] 63.18 μm and [C II] 157.74 μm are normalized to the FIFI-LS maximum luminosity. X-axis shows the offset from the adopted center of DR21 Main ($20^{\text{h}}39^{\text{m}}00^{\text{s}}.93$, $+42^{\circ}19'42''$).

Table 3: Ratios of line luminosities in units of L_{\odot} inside each box along the outflow major axis of DR21 Main (Fig. 7)

Box	Offset	[O I] 63/145	[O III] 52/88	[O I] 63/[C II]	[O I] 145/[O III]52	CO 14-13/16-15	CO 16-15/OH
1	(69.7,28.6)	10.34 ± 4.14	0.97 ± 0.39	4.61 ± 1.85	3.85 ± 1.54	1.18 ± 0.47	15.50 ± 6.20
2	(54.1,22.2)	6.26 ± 2.50	0.78 ± 0.31	3.07 ± 1.23	2.75 ± 1.10	1.39 ± 0.56	7.99 ± 3.20
3	(38.6,15.8)	9.75 ± 3.90	1.34 ± 0.54	5.09 ± 2.04	0.62 ± 0.25	0.99 ± 0.39	4.13 ± 1.65
4	(23.0,9.4)	9.29 ± 3.72	1.41 ± 0.57	5.42 ± 2.17	0.40 ± 0.16	0.83 ± 0.33	4.00 ± 1.60
5	(7.5,3.1)	6.91 ± 2.76	1.22 ± 0.49	4.71 ± 1.88	0.52 ± 0.21	1.07 ± 0.43	5.48 ± 2.19
6	(-8.1,-3.3)	10.32 ± 4.13	1.01 ± 0.40	5.44 ± 2.18	0.93 ± 0.37	0.93 ± 0.37	6.50 ± 2.60
7	(-23.6,-9.7)	13.28 ± 5.31	0.59 ± 0.24	4.95 ± 1.98	3.40 ± 1.36	0.81 ± 0.32	8.85 ± 3.54
8	(-39.1,-16.1)	14.54 ± 5.81	0.81 ± 0.32	4.40 ± 1.76	2.83 ± 1.13	0.89 ± 0.36	9.81 ± 3.92
9	(-54.7,-22.5)	14.70 ± 5.88	1.22 ± 0.49	5.30 ± 2.12	3.53 ± 1.41	1.34 ± 0.54	4.52 ± 1.81
10	(-70.2,-28.8)	18.57 ± 7.43	2.17 ± 0.87	7.75 ± 3.10	2.28 ± 0.91	1.38 ± 0.55	6.92 ± 2.77

Notes. Uncertainties include statistical error associated with absolute flux calibration.

to assess the physical conditions that could reproduce the observed ratio of CO lines.

Figure 8 shows the ratio of the CO 14-13 and 16-15 lines for H_2 densities of $n(H_2) = 10^4 - 10^8 \text{ cm}^{-3}$ and kinetic temperatures of $T_{\text{kin}} = 10^2 - 2 \times 10^3$ obtained using RADEX (van der Tak et al. 2007). In addition, Figure 4 shows the comparison of the models to observations for T_{kin} of 200, 300, 500, and 1000 K. The line width of 40 km s^{-1} is taken from resolved line profiles of CO 7-6 (Jakob et al. 2007) and ^{13}CO 10-9 (van der Tak et al. 2010). The column density of 10^{17} cm^{-2} is chosen such that the emission is optically thin. The collisional rate coefficients for CO lines with J up to 60 are from Yang et al. (2010) and Neufeld (2012).

The observed CO line ratio can be described by a range of physical conditions, which can be divided into two limiting solutions: (i) low-density, $n(H_2) \lesssim n_{\text{crit}}^{\text{CO}}$, high-temperature of $T_{\text{kin}} \gtrsim 10^3 \text{ K}$ regime; or (ii) high-density, $n(H_2) \gtrsim n_{\text{crit}}^{\text{CO}}$, moderate temperature of $T_{\text{kin}} \gtrsim 10^2 - 10^3 \text{ K}$ regime, corresponding to LTE conditions. The degeneracy between those solutions cannot be solved by CO observations alone; however, the bright emission of the DR21 Main outflow in vibrationally-excited H_2 requires gas densities above 10^5 cm^{-3} (Garden et al. 1986; Davis et al. 2007). In addition, modeling of mid- J CO and HCO^+ lines sug-

gests gas densities in excess of 10^6 cm^{-3} toward the center of DR21 Main (Ossenkopf et al. 2010). Therefore, we favor the high-density scenario, in which CO line ratios depend mostly on the changes in T_{kin} along the outflow (Fig. 4). The values of T_{kin} along the outflow for the H_2 densities of 10^4 , 10^5 , and 10^6 cm^{-3} are shown in Table 4.

4.2.2. Atomic gas component

For optically-thin lines excited under LTE conditions, excitation temperature of the atomic gas, $T_{\text{exc}}^{[\text{O I}]}$, can be expressed as:

$$T_{\text{exc}}^{[\text{O I}]} = 98.87 \times \ln^{-1}(0.0284 \times R_{[\text{O I}]}) \quad \text{for } R_{[\text{O I}]} > 35.2 \quad (2)$$

where $R_{[\text{O I}]}$ refers to the luminosity ratio of the [O I] lines at 63.18 and 145.53 μm , and the atomic data is taken from Table 1. The observed ratio of the [O I] lines, with a mean of 10.4 ± 3.8 (Table 3), falls in the range where Eq. 2 is, however, not applicable. The non-LTE radiative-transfer models also predict higher ratios of the [O I] lines in the optically-thin regime (Fig. 8).

The discrepancy between models and observations might be due to line-of-sight absorption or high optical depth of the [O I] lines. We quantified the impact of absorption on the [O I] 63.18

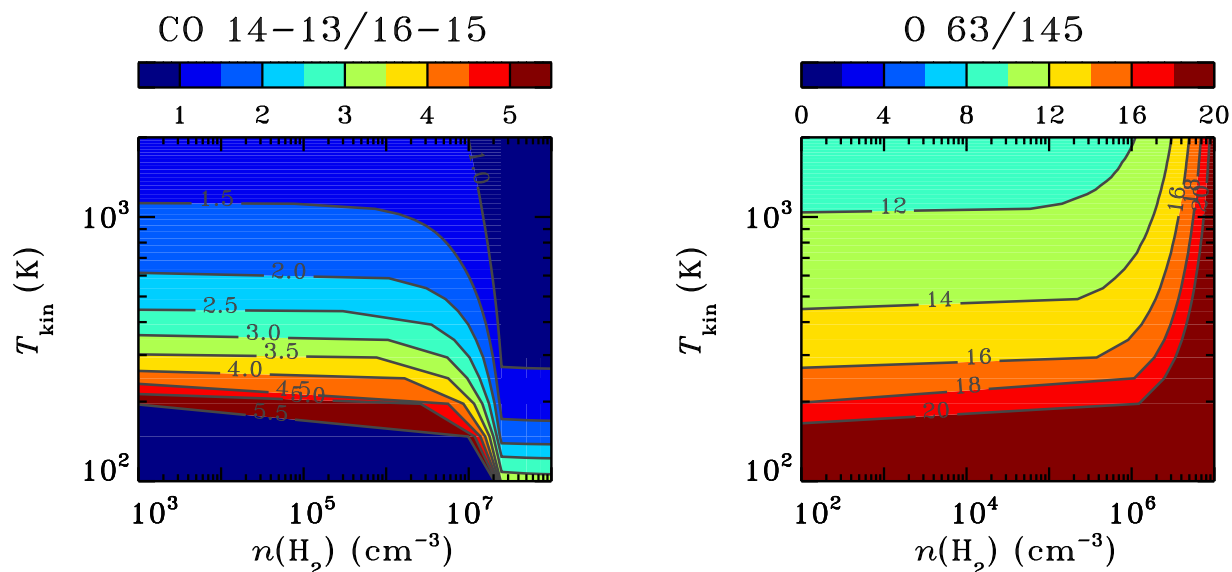


Fig. 8: Ratio of line fluxes of two CO (left) and two [O I] lines (right) as a function of H₂ density and kinetic temperature of the emitting gas derived from non-LTE excitation calculations. The assumed column densities of CO and atomic oxygen of 10¹⁷ cm⁻² and line width of 40 km s⁻¹ result in optically-thin emission.

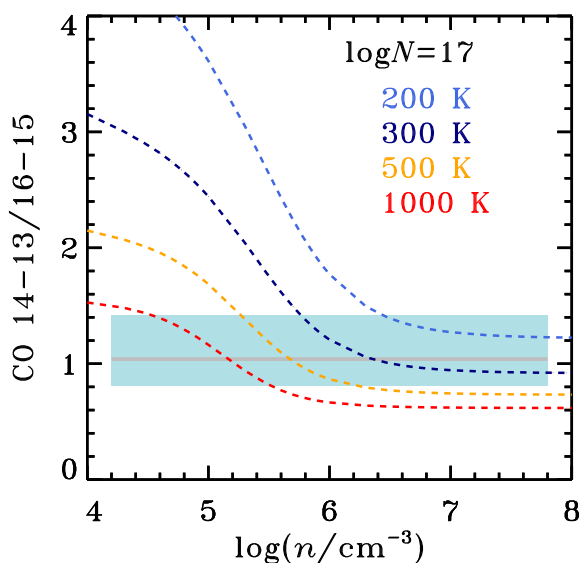


Fig. 9: Ratio of line fluxes of CO 14-13 and CO 16-15 as a function of logarithm of H₂ density. Lines show non-LTE radiative-transfer models for gas kinetic temperatures of 200 K (light blue), 300 K (blue), 500 K (orange), and 1000 K (red), assuming collisions with H₂. The observations are shown as light blue boxes with the horizontal grey line indicating the median values of ratios for all boxes along the DR21 outflow.

μm line in Section 3.2; here, we will assume that the [O I] 145.53 μm line is not equally affected by absorption due to higher den-

Table 4: Kinetic temperatures and densities from CO lines

Box	T_{kin} (K)			
	$n_{\text{H}} = 10^4 \text{ cm}^{-3}$	10^5 cm^{-3}	10^6 cm^{-3}	10^7 cm^{-3}
1	1750-2000	800-1250	300-350	200-250
2	1000-2000	600-850	250	200
3	≥ 2000	1200-2000	350-450	250-300
4	≥ 2000	1900-2000	500-650	350-450
5	≥ 2000	1000-1600	350-400	250
6	≥ 2000	1400-2000	400-500	300-350
7	≥ 2000	≥ 2000	500-700	350-500
8	≥ 2000	1600-2000	450-550	300-400
9	1150-2000	650-900	250-300	200
10	1050-2000	600-850	250	200

Notes. The calculations assumed a column density of CO of 10¹⁷ cm⁻² and a line width of 40 km s⁻¹ (see Section 4.2.1). The ranges of T_{kin} are provided assuming the 10% error of the CO 14-13/CO 16-15 ratio. The temperature of 2000 K is the maximum value in our grid (Fig. 8) and should be considered as the lower limit at low-densities.

sities needed for line excitation. To verify the impact of optical depths, we calculate RADEX models for a broad range of oxygen column densities of 10¹⁷, 10¹⁹, and 10²¹ cm⁻² (Fig. 10) and the line width of 40 km s⁻¹. The collisional rate coefficients for [O I] lines, both for collisions with H₂ and H, are taken from Lique et al. (2018). The corresponding critical densities of the [O I] 63.18 μm line are $2.9 \times 10^5 \text{ cm}^{-3}$ for collisions with o-H₂, and $2.4 \times 10^5 \text{ cm}^{-3}$ for collisions with H, assuming T_{kin} of 220 K. For the [O I] 145.53 μm line, the critical densities are about an order of magnitude higher for collisions with o-H₂ ($2.8 \times 10^6 \text{ cm}^{-3}$), and comparable to those of the 63.18 μm line for collisions with H ($1.3 \times 10^5 \text{ cm}^{-3}$).

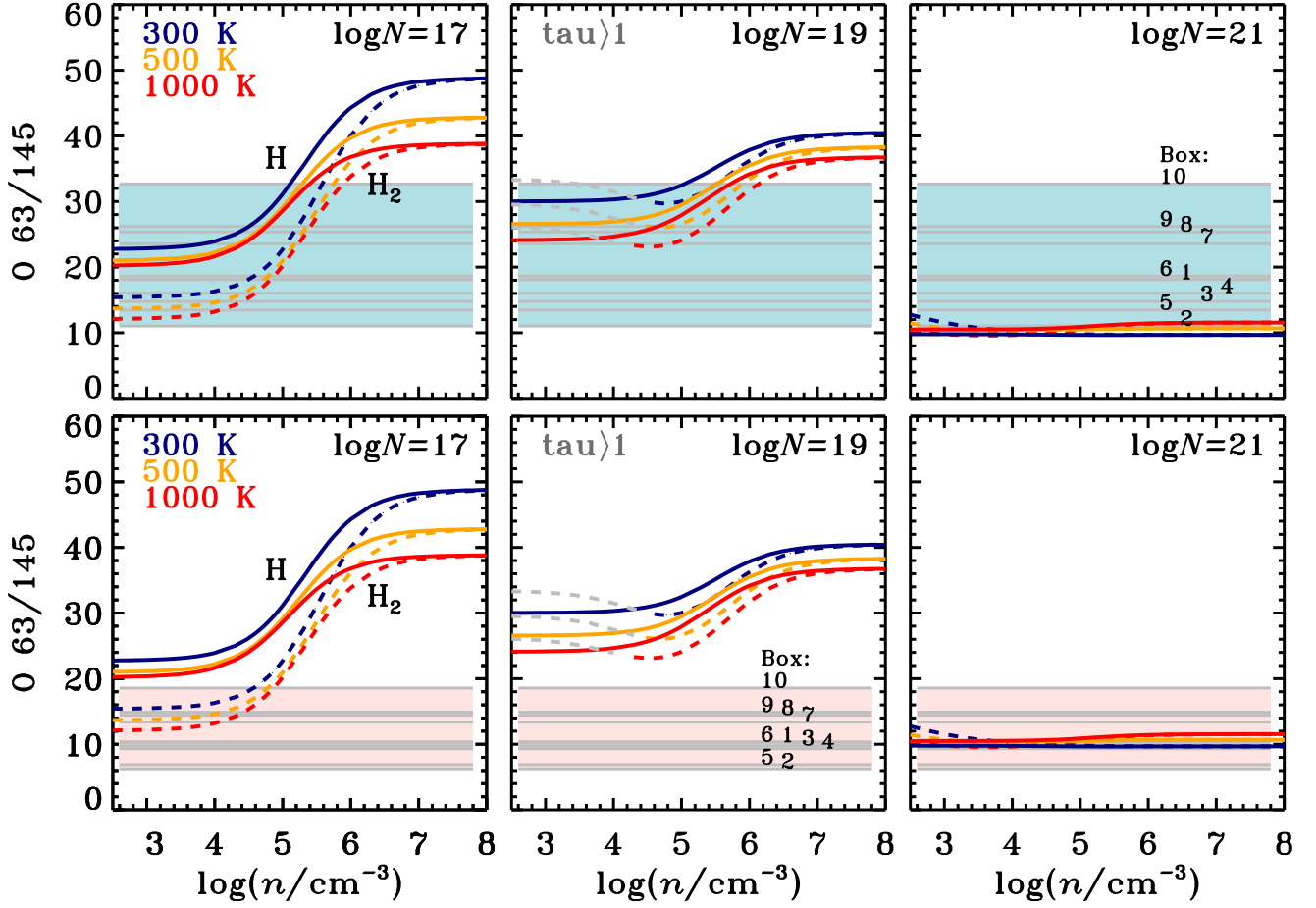


Fig. 10: Ratio of line fluxes of [O I] 63.18 and 145.53 μm as a function of the logarithm of hydrogen density. Lines show non-LTE radiative-transfer models for gas kinetic temperatures of 300 K (blue), 500 K (orange), and 1000 K (red), assuming collisions with atomic (solid lines) and molecular hydrogen (dashed lines). Models are calculated for oxygen column densities of 10^{17} cm^{-2} (left), 10^{19} cm^{-2} (center), and 10^{21} cm^{-2} (right). The observations corrected for absorption in the [O I] 63.18 μm line are shown as light blue boxes (top panel), and uncorrected ones as rose boxes (bottom panel). The horizontal gray lines indicate ratios for specific boxes along the DR21 outflow.

The three panels in Fig. 10 correspond to three regimes in the optical depth of the [O I] lines, where: (i) both lines are optically thin at N of 10^{17} cm^{-2} ; (ii) the [O I] 63.18 μm line is optically thick, and the 145.53 μm line is optically thin at N of 10^{19} cm^{-2} ; (iii) both lines are optically thick at N of 10^{21} cm^{-2} . The results for N of 10^{17} cm^{-2} are qualitatively similar to radiative-transfer models of [O I] emission toward outflows from low-mass protostars (Liseau et al. 2006; Nisini et al. 2015; Yang et al. 2022). In this regime, H_2 densities below $10^4 - 10^5 \text{ cm}^{-3}$ and T_{kin} between 300-1000 K reproduce the observed ratios (both corrected and uncorrected for the absorption in the [O I] 63.18 μm line). The models assuming collisions with H reproduce only the absorption-corrected ratios from observations, providing about an order of magnitude lower densities than the absorption-corrected match for the collisions with H_2 . Both oxygen lines are also optically thin for N of 10^{18} cm^{-2} , with model predictions resulting in slightly higher ratios of the [O I] 63.18/145.53 μm lines.

For oxygen column densities of 10^{19} cm^{-2} , neither collisions with H_2 nor with H can reproduce the observed range of the [O I] line ratios from FIFI-LS (Fig. 10). When the [O I] line at 63.18 μm is absorption-corrected, the models reproduce the observations for H/ H_2 densities below 10^6 cm^{-3} and T_{kin} between 300-1000 K. The [O I] line at 63.18 μm is optically-thick ($\tau \geq 1$) for H_2 densities either below 10^4 cm^{-3} or of $3 - 4 \times 10^4 \text{ cm}^{-3}$ at kinetic temperatures of 1000 K and 300 K, respectively, and optically thin for regions where collisions with atomic hydrogen dominate the excitation. The [O I] line at 145.53 μm is optically-thin in the considered regimes of temperature and densities (of both H and H_2) due to its higher critical densities.

For oxygen column densities equal to or above 10^{20} cm^{-2} , both oxygen lines are optically-thick. For N of 10^{20} cm^{-2} , τ of the 63.18 μm line is always ≥ 1 (both for collisions with H and H_2). The 145.53 μm line becomes optically thick for the H_2 densities below $8 \times 10^5 \text{ cm}^{-3}$ and $2 \times 10^4 \text{ cm}^{-3}$ at 300 K and 1000 K, respectively. For N of 10^{21} cm^{-2} , both lines are optically-thick

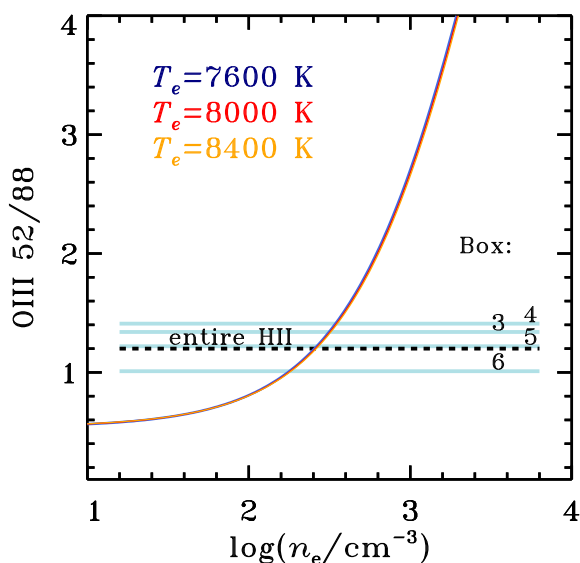


Fig. 11: Ratio of line fluxes of [O III] lines at 52 and 88 μm in units of $\text{erg cm}^{-2} \text{s}^{-1}$ as a function of logarithm of electron density. Lines show non-LTE radiative-transfer models for a gas electron temperature of 8000 ± 400 K derived from the GLOSTAR survey (Khan et al. 2024). The observed ratios toward the boxes 3-6 along the DR21 outflow, where both [O III] lines are firmly detected, are shown in light blue lines, and for the area of the H II region in GLOSTAR (see Fig. 4) in dashed black line.

Table 5: Electron densities from [O III] lines

Box	n_e (cm^{-3})		
	$T_e=7600$ K	8000 K	8400 K
3	270–380	270–360	270–380
4	300–410	290–390	300–410
5	220–310	220–310	220–320
6	140–220	140–210	140–220
Entire HII	210–300	210–300	220–310

Notes. T_e of 8000 ± 400 K was obtained as part of the GLOSTAR survey (Khan et al. 2024). The ranges of T_e are provided assuming the 10% error of the [O III] 52/88 μm ratio.

for the entire range of considered physical conditions, and their observed absorption-corrected ratios are well-above the modeled ratios (Fig. 10).

To summarize, when we adopt the correction factor obtained from the velocity-resolved observations that accounts for absorption in the [O I] 63.18 μm line (Section 3.2), the observed line ratios agree best with non-LTE models assuming an oxygen column density of 10^{17}cm^{-2} and optically thin lines (left panel of Fig. 10). However, larger oxygen column densities ($\sim 10^{19} \text{cm}^{-2}$) might be present at certain locations (Poglitsch et al. 1996), implying higher gas densities. The upcoming full analysis of all upGREAT spectra will provide better constraints on the column densities (Ossenkopf, in preparation).

4.2.3. Ionized gas component

Electron densities in the central H II regions of DR21 Main can be quantified using the two transitions of ionized oxygen, the [O III] lines at 51.81 and 88.35 μm , whose critical densities for collisions with electrons are 4000 and 510 cm^{-3} , respectively (Beck et al. 2022, and references therein). Even though the [O III] line ratio is most sensitive to the density of ionized gas, we consider a range of electron temperatures, T_e , obtained toward DR21 Main using radio recombination lines from the literature.

We calculate electron densities in the H II regions using the Python package PyNeb, which solves the equilibrium equations of the n-level atom and determines the level populations (Luridiana et al. 2015), see also a description of the procedure in Beck et al. (2022). We assumed three values of T_e : from 7000 to 9000 K in steps of 1000 K, consistent with the most recent estimate of 8000 ± 400 K toward DR21 Main from the GLOSTAR survey (Khan et al. 2024). Noteworthy, those values are also consistent with the T_e measured across DR21 Main using Very Large Array observations, which provided the average value of T_e of 7500 K (Roelfsema et al. 1989).

Figure 11 shows the comparison of the models with the FIFI-LS measurements of the [O III] line ratio along the outflow of DR21 Main. The range of best-fit electron densities corresponding to the area of the H II region covered by GLOSTAR (Fig. 4) equals 240–280 cm^{-3} for T_e in the range of 7600 to 8400 K, corresponding to the uncertainties of T_e from GLOSTAR (see Table 5 and Section 5.1). A somewhat broader range of densities of 140–410 cm^{-3} is obtained for boxes 3-6 (Fig. 11).

Electron densities determined from the [O III] lines are a factor of 3 lower than n_e obtained from VLA in the so-called low-density regions toward DR21 Main (Roelfsema et al. 1989), likely due to differences in the resolution.

4.3. Molecular and atomic line cooling

Emission in the far-IR molecular and atomic lines provides important constraints on the physical processes that are responsible for the heating and cooling of the gas. For example, CO and H₂O are key gas cooling channels of non-dissociative shocks associated with the outflows (Kaufman & Neufeld 1996; Flower & Pineau Des Forêts 2010), and [C II] and [O I] emission is enhanced in dissociative shocks (Hollenbach & McKee 1989; Neufeld & Dalgarno 1989) and PDRs (Tielens & Hollenbach 1985; Kaufman et al. 1999). The total gas cooling budget, when dominated by the outflow, serves as a direct measure of mechanical luminosity deposited by the outflow (Maret et al. 2009; Karska et al. 2018).

Table 6 shows the line luminosities of far-IR species obtained for each box along the DR21 Main outflow (see also Section 4.1). Individual line luminosities and total cooling (L_{tot}) are obtained directly from FIFI-LS measurements, and the far-IR line cooling (L_{FIRL} , see below) accounts for the absorption in the [O I] 63.18 μm line. The total line luminosity of [O I], $L_{[\text{O I}]}$, is determined from a sum of line luminosities of the two far-IR transitions; the same is done for [O III]. The total line luminosity of CO, L_{CO} , is extrapolated from the observed transitions using the CO excitation temperature determined from the CO 14-13 and 16-15 transitions (Section 4.2.1). Here, we account for CO transitions from the upper rotational levels $J_{\text{u}} = 14 - 24$ ($E_{\text{u}} \sim 580 - 1660$ K), corresponding to the “warm” component on CO rotational diagrams of low-mass protostars, which is characterized by median T_{rot} of ~ 320 K (Karska et al. 2018) and also

Table 6: Far-IR line cooling in units of L_{\odot}

Box	$L_{[\text{O I}]}$	$L_{[\text{C II}]}$	$L_{[\text{O III}]}$	L_{OH}	L_{CO}	$L_{\text{CO}}^{\text{tot}}$	L_{tot}	L_{FIRL}
1	9.47±1.89	1.87±0.37	0.44±0.09	0.02±0.0	0.33±0.07	1.05±0.21	12.42±2.48	17.11±3.21
2	7.42±1.48	2.09±0.42	0.84±0.17	0.03±0.01	0.28±0.06	0.92±0.18	10.45±2.09	13.22±2.46
3	11.32±2.26	2.02±0.4	2.95±0.59	0.09±0.02	0.35±0.07	1.59±0.32	15.02±3.0	18.24±3.34
4	13.21±2.64	2.2±0.44	5.51±1.1	0.16±0.03	0.58±0.12	3.41±0.68	18.99±3.8	25.37±4.41
5	15.33±3.07	2.84±0.57	6.73±1.35	0.24±0.05	1.36±0.27	5.06±1.01	23.47±4.69	33.35±5.68
6	14.88±2.98	2.49±0.5	2.81±0.56	0.23±0.05	1.42±0.28	6.55±1.31	24.14±4.83	32.5±5.21
7	8.05±1.61	1.51±0.3	0.45±0.09	0.08±0.02	0.61±0.12	3.19±0.64	12.84±2.57	17.01±2.77
8	4.78±0.96	1.02±0.2	0.24±0.05	0.02±0.0	0.2±0.04	0.88±0.18	6.7±1.34	9.08±1.64
9	5.09±1.02	0.9±0.18	0.17±0.03	0.07±0.01	0.37±0.07	0.99±0.2	7.04±1.41	9.76±1.76
10	4.49±0.9	0.55±0.11	0.15±0.03	0.06±0.01	0.46±0.09	1.14±0.23	6.25±1.25	8.94±1.56
Sum	94.04±18.81	17.49±3.5	20.3±4.06	0.98±0.2	5.97±1.19	24.79±4.96	137.3±27.46	184.59±32.06

Notes. $L_{[\text{O I}]}$ and $L_{[\text{O III}]}$ are the sums of line luminosities of two lines of atomic and ionized oxygen, respectively. $L_{[\text{C II}]}$ is obtained from the line flux of [C II] line at $157.7 \mu\text{m}$, and L_{OH} from the line flux of the OH line at $163.13 \mu\text{m}$ line. L_{CO} is the sum of line luminosities of the CO 14-13 and 16-15 lines. $L_{\text{CO}}^{\text{tot}}$ refers to the extrapolated total CO line luminosity in the far-IR range ('warm component', see Section 4.3). L_{tot} refers to the total far-IR line emission from FIFI-LS, whereas L_{FIRL}^* accounts for the absorption in the [O I] and does not contain the emission from the [C II] line. Uncertainties include statistical error associated with absolute flux calibration.

consistent with rotational temperatures of high-mass protostars (Karska et al. 2014a; Hoang et al. 2023). The total line luminosity of OH is calculated by multiplying the flux of the OH line at $163.13 \mu\text{m}$ by a factor of two, to account for the second, unobserved component of the doublet at $163.4 \mu\text{m}$. This OH doublet is often the only one that is detected in emission toward high-mass protostars (Wampfler et al. 2011, 2013; Leurini et al. 2015; Csengeri et al. 2022); therefore we do not account for the remaining lines as possible contributors to the line cooling (Karska et al. 2014a).

We define the far-IR line cooling (L_{FIRL}) as the sum of line luminosities of the [O I] lines and detected molecules:

$$L_{\text{FIRL}} = L_{[\text{O I}]} + L_{[\text{C II}]} + L_{\text{CO}}^{\text{tot}} + L_{\text{OH}}. \quad (3)$$

For consistency with previous studies of deeply-embedded protostars, we exclude cooling in [O III] lines and [C II] from L_{FIRL} (Karska et al. 2013). The [O III] emission predominately traces the H II regions, whereas [C II] is strongly associated with the PDRs (Section 4.2.3). H_2O lines were not observed with SOFIA, so we also exclude them from the original formula for L_{FIRL} adopted in Nisini et al. (2002) and Karska et al. (2013). However, for the sake of possible comparisons with extragalactic star-forming regions and general overview, we also report the total gas cooling, L_{tot} , defined as:

$$L_{\text{tot}} = L_{\text{FIRL}} + L_{[\text{C II}]}. \quad (4)$$

Relative contributions of each species to L_{tot} are shown in Figure 12. The cooling in [O I] lines is dominant, and accounts for ~62-76% of the total far-IR line cooling along the DR21 Main outflow. Its highest contributions to L_{tot} , above 70%, are measured in the outflow-lobes, whereas lower values of ~62-65% are obtained in the center, likely due to unresolved absorption in the [O I] $63.18 \mu\text{m}$ line (see also Section 4.2.2). The second most important gas coolant, CO, accounts for ~8-27% of L_{tot} as measured in the center of DR21 Main, and is likely not affected by absorption. In the outflow lobes, $L_{\text{CO}}^{\text{tot}}$ ranges from ~8-11% in the eastern to ~13-18% in the western outflow-lobe (Fig. 12). Finally, the gas cooling in [C II] accounts for ~9-20%, and in OH for 0.2-1.0% of L_{tot} . A possible contribution of H_2O , not observed with FIFI-LS, is expected to account for less than

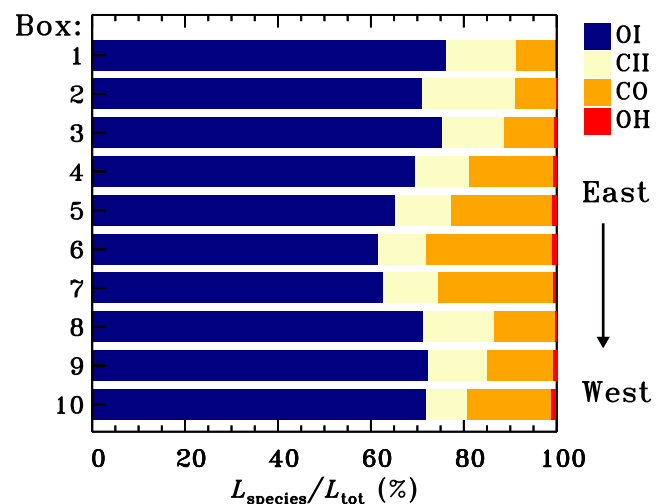


Fig. 12: Relative contributions of [O I] (dark blue), [C II] (yellow), CO (orange), and OH (red) cooling to the total far-IR gas cooling are shown from left to right horizontally for each box along the DR21 outflow. The boxes are drawn from E to W, with the western outflow-lobe on top.

10% of L_{tot} (Karska et al. 2014a). We discuss the line cooling in DR21 Main in the context of other high-mass protostars in Section 5.3.

In summary, the far-IR line cooling along the outflow of DR21 Main is most likely dominated by [O I], and to a lesser extent by high- J CO lines. The apparent decrease of [O I] luminosity in the central region is at least partly due to foreground absorption unresolved with FIFI-LS.

5. Discussion

DR21 Main contains several physical components associated with spatially-resolved FIFI-LS observations of far-IR emission:

i) a bipolar outflow seen in full extent in the [O I] 63.18 μm and the high- J CO lines; ii) central H II regions producing a PDR associated with bright CO, OH, [C II], [O I], and [O III] emission; iii) outflow cavities in the eastern outflow lobe, best traced by atomic and ionic lines, and iv) interaction region in the western outflow lobe, associated with dense gas and peaks of CO and OH emission (Section 3). The components differ in gas physical conditions such as temperature, density, UV radiation fields, and ionization, as revealed by the change of their line ratios along the outflow direction (Section 4). Combined with velocity information from other line tracers and physical-chemical models of molecular excitation, far-IR data might inform the dominant underlying physical processes along the DR21 Main outflow.

Bright and extended H₂ emission is clearly the most remarkable feature of DR21 Main, which strongly suggest shocks along the outflow (component i, Garden et al. 1986; Smith et al. 1998; Cruz-González et al. 2007; Davis et al. 2007). A similar pattern of emission has been detected in low- J CO and HCO⁺ lines, which trace the bulk of the outflow mass (Garden et al. 1990; Skretas et al. 2023). In addition, the spatial distribution of the [O I] 63.18 μm line and its broad line wings measured with the Fabry-Perot instrument at KAO hinted at its link to the outflow (Poglitsch et al. 1996). Yet, the analysis of emission in multiple tracers was inconsistent with standard shock models, and pointed at the origin of far-IR emission in the warm, dense PDRs (Lane et al. 1990; Jakob et al. 2007).

The impact of UV radiation is expected to be strongest at the center of DR21 Main (component ii), hosting at least six OB stars (Roelfsema et al. 1989) and two cometary H II regions, created as the result of the motion of ionizing stars through the dense molecular cloud (Cyganowski et al. 2003). The region consists of UV-irradiated dense clumps indicated by the bright PAH emission in the 8 μm images from *Spitzer*/IRAC (Marston et al. 2004). Detailed modeling of velocity-resolved lines of [C II], HCO⁺, and high- J CO isotopologues from single-pointing *Herschel*/HIFI observations revealed two PDR ensembles: (a) a hot and compact component associated with the inner part of the H II regions with G_0 of $\sim 1.7 \times 10^5$; (b) a cooler, extended component with G_0 of $\sim 5.4 \times 10^2$ (Ossenkopf et al. 2010). At the same time, H₂O observations over the same spatial scales show high-velocity wings due to outflow, which clearly affects the dynamics and physical conditions in the central parts of DR21 (van der Tak et al. 2010, see also Ashby et al. 2000).

Ionized gas was also spatially-resolved in the eastern, elongated part of the cometary H II region (component iii) in the [N II] line using *Herschel*/SPIRE (White et al. 2010). This area shows extended emission of the H I 21 cm line (Russell et al. 1992) and is co-spatial with the cavity of H₂ emission in the eastern outflow lobe (Cruz-González et al. 2007). It also showed several spots of H₂O masers (Plambeck & Menten 1990), which are associated with dissociative shocks (Hollenbach et al. 2013). White et al. (2010) used the ratio of the [N II] and [C II] line to obtain the lower limit of $\sim 30 \text{ cm}^{-3}$ for the gas density of ionized gas using [C II] measurements from ISO/LWS (Jakob et al. 2007). Our FIFI-LS observations provide the highest-resolution image of this cavity of ionized gas to date (Section 3), supporting the early interpretation of the origin of H I as a result of recombination of the initially ionized outflow component (Russell et al. 1992).

Such ionized gas is not detected in the western outflow lobe, which is mainly associated with the emission from H₂ (Garden et al. 1986; Davis et al. 2007) and CO (Garden et al. 1990). A recent multi-tracer study using IRAM 30m and NOEMA characterized the interaction region (component iv), finding a spa-

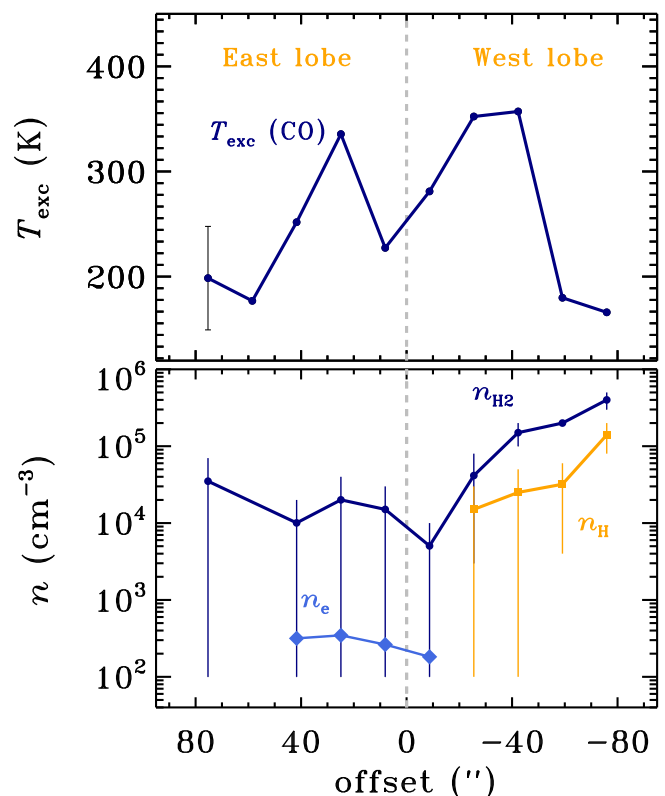


Fig. 13: Physical conditions along the DR21 Main outflow: CO excitation temperature (top) and gas densities (bottom). The CO excitation temperature is obtained from the ratio of CO 14-13 and 16-15 lines at 185.99 μm and 162.81 μm , respectively (see Section 4.2.1). A typical errorbar is shown for the offset of 80". The H₂, H, and e densities are estimated assuming the oxygen column density of 10^{17} cm^{-2} , in regions where sufficient agreement with observations was found (Section 4.2.2). Gas temperature of 300 K, consistent with $T_{\text{rot}}(\text{CO})$, was further assumed for the H₂ and H emitting gas. Vertical lines show the ranges of densities in agreement with models, whereas the symbols refer to the average values at a given offset.

tially stratified emission from the 1-0 transitions of SiO, H₂CO, CH₃OH, DCN, DCO⁺, DNC, and NH₂D (Skretas et al. 2023). The qualitative comparison of observations to the chemistry of shocked regions confirmed the presence of ongoing interaction between the DR21 Main outflow and a dense clump, initially suggested by the detection of a collisionally excited Class I methanol maser in the same area (Plambeck & Menten 1990).

In the following subsections, we discuss the high-resolution far-IR observations from SOFIA FIFI-LS in the context of gas physical conditions and underlying processes along the DR21 Main outflow. As we will see, a new generation of shock models including the impact of UV irradiation can explain the observed far-IR line spectrum of DR21 Main for the first time. We will also explore the overall outflow energetics and compare it to the estimates from the submillimeter survey CASCADE (Skretas et al. 2023).

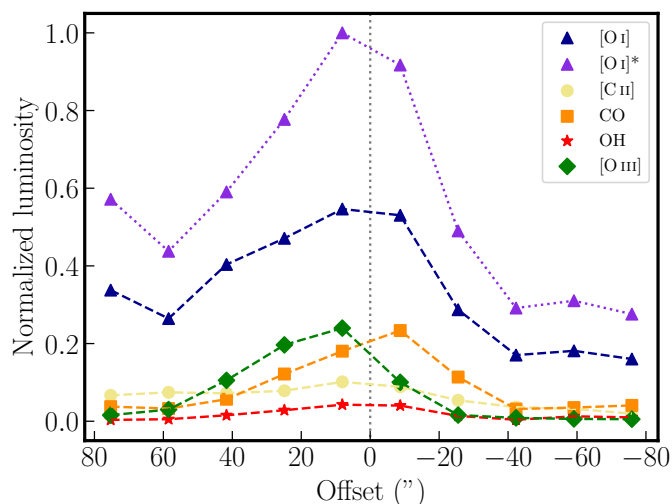


Fig. 14: Line luminosities of far-IR lines along the DR21 Main outflow. The absorption-corrected luminosity of $[O\text{I}]$ is shown in violet and the measured values from FIFI-LS in blue. The total line luminosities of $[C\text{II}]$, CO, OH, and $[O\text{III}]$ are in yellow, orange, red, and green, respectively. They are normalized to the total luminosity of absorption-corrected $[O\text{I}]$ luminosity – $[O\text{I}]^*$. In addition, OH is scaled up by a factor of 5 for better visualization. X-axis shows the offset from the adopted center of DR21 Main, see also Fig. 7.

5.1. Origin of the far-IR emission: DR21 Main outflow

The comparison of far-IR emission in various species is a powerful tool to constrain the physical conditions and the underlying physical processes in star-forming regions (Herczeg et al. 2012; Karska et al. 2013; Green et al. 2016; Yang et al. 2018). In this section, we investigate the changes of gas physical conditions and far-IR line cooling along the outflow of DR21 Main and test the observed emission against shock models.

Bright emission in high- J CO and H_2O is known to be produced by models of non-dissociative C-type shocks, which compress and heat the gas during the passage of the outflow and cool primarily by molecular emission (Kaufman & Neufeld 1996; Bergin et al. 1998; Flower & Pineau Des Forêts 2010). Yet, such models do not reproduce neither the relatively high line ratios of OH over H_2O (Karska et al. 2014b) nor the velocity-resolved emission from light (ionized) hydrides toward low- and high-mass protostars (Kristensen et al. 2013; Benz et al. 2016). They also fail to reproduce bright $[O\text{I}]$ and $[C\text{II}]$ emission, which was the main argument to dismiss them in the context of DR21 Main (Lane et al. 1990).

Recent observations with *Herschel* inspired the development of a new generation of C-type shocks models, which include irradiation by UV-photons (Melnick & Kaufman 2015; Godard et al. 2019). The impact of UV photons concerns both the shock structure and the abundances of key cooling species, thereby explaining the observed far-IR spectra of low-mass protostars (Kristensen et al. 2017; Karska et al. 2018). In the case of DR21 Main, it is expected that UV radiation young stars located in the center of the region affects the chemical composition of the outflow and its far-IR emission. Roelfsema et al. (1989) identified 6 O-type stars (see Fig. 1), and estimated that their ionizing radiation corresponds to those of ~ 11 O8 stars.

The analysis of far-IR line ratios presented in Section 4 confirms significant differences of physical conditions along the

DR21 Main outflow. CO rotational temperatures, which are a good proxy of gas kinetic temperature, are highest in the outflow lobes (Figure 13, upper panel). Molecular gas densities, as determined from the $[O\text{I}]$ line ratios (Sect. 4.2.2), of up to a few $\times 10^5\text{ cm}^{-3}$ are estimated in the western outflow lobe (Figure 13, lower panel). Those H_2 densities are about an order of magnitude higher than in the region of H_2 enhancement in the eastern outflow lobe. They are consistent with the high-density solution of CO excitation (Sect. 4.2.1) and with earlier estimates pin-pointing the differences in gas densities between the eastern and western outflow lobes of DR21 Main (e.g., Russell et al. 1992).

Assuming that the main collisional partner of O is H, the H densities agree with radiative-transfer models only for the western outflow lobe, and show a trend similar to that assuming H_2 collisions. The densities of ionized gas of the order of a few $\times 10^2\text{ cm}^{-3}$ are estimated in the ionized cavity wall, consistent with ISO measurements using the same lines (Jakob et al. 2007).

Stratification of gas physical conditions along the DR21 Main outflow is closely reflected in the relative importance of gas cooling in various far-IR species. Figure 14 shows the total luminosities of each species as a function of the distance from the center of DR21 Main normalized to the luminosity of $[O\text{I}]$ (see also Section 4.1). The patterns are qualitatively similar to those shown in Fig. 7: the luminosity of atomic and ionized oxygen, and to a smaller extent $[C\text{II}]$, dominates in the eastern outflow-lobe, whereas the luminosity of high- J CO and OH are stronger in the western outflow-lobe (see also Section 4.1). In absolute terms, the total far-IR line cooling is a factor of ~ 2 higher in the eastern outflow-lobe than in the western part of the outflow. Even higher gas cooling originates from the central region of DR21 Main, which overlaps with the HII regions.

We use the ratios of far-IR species which are most likely dominated by the emission from the outflow to constrain the underlying shock parameters. In addition, we account for the impact of UV photons, which are expected to influence the molecular emission in both low-mass (van Kempen et al. 2010; Visser et al. 2012; Yıldız et al. 2015), and high-mass protostars (Bruderer et al. 2009; Benz et al. 2016). We adopt model predictions for UV-irradiated C-shocks, characterized by a range of UV field strengths, G_0 , of 0.1, 1, and 10 (Melnick & Kaufman 2015; Karska et al. 2018). Noteworthy, UV fields in the central region of DR21 Main might be even a few orders of magnitude higher, $G_0 \sim 10^5$ (Ossenkopf et al. 2010), due to irradiation from O-type stars at the center of DR21 Main. This is, however, unlikely the case for the outflow component associated with higher gas densities, where UV radiation is more readily attenuated by dust grains. Using dust continuum maps from *Herschel*, we estimate that the UV field decreases below $\sim 10^3$ at the interaction region of DR21 Main (Appendix D). UV fields produced by shocks that do not dissociate CO are of the order of tens of the average interstellar radiation field (van Kempen et al. 2009). This is likely the case of DR21 Main, since the West part of the outflow is not associated with the enhancement of the $[C\text{II}]$ emission (Fig. 3).

Figure 15 shows the comparison of the model ratios of the $[O\text{I}]$ 63.18 μm and OH 163.13 μm lines over total CO luminosities and the observations along the DR21 Main outflow. Qualitatively, shock models spanning a range of velocities (10-20 km s^{-1}) and UV fields ($G_0 = 0.1 - 10$) agree with the measurements from FIFI-LS. Higher ratios of the $[O\text{I}]$ and CO lines, observed in the eastern outflow lobe, correspond to the models with lower pre-shock gas densities of 10^3 - 10^4 cm^{-3} , as suggested by earlier works (Russell et al. 1992; Lane et al. 1990). On the contrary, lower $[O\text{I}] / \text{CO}$ ratios are consistent with the pres-

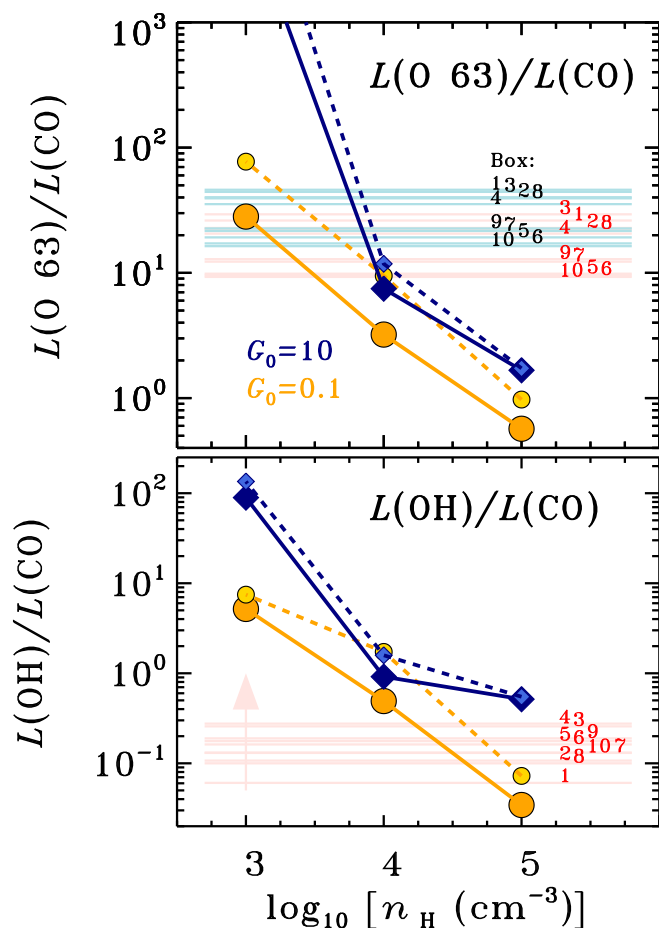


Fig. 15: Ratio of the [O I] 63.18 μm and CO luminosities (top) and the OH and CO luminosities (bottom) as a function of pre-shock velocity for UV irradiated C-shock models and observations of DR21 Main. All models correspond to UV fields parameterized by G_0 of 10 (in blue) and 0.1 (in orange). Solid lines connect models with shock velocities v_s of 20 km s^{-1} , and dashed lines – the models with v_s of 10 km s^{-1} . Observations for specific boxes along the DR21 outflow are shown as horizontal lines: in pink are measurements from FIFI-LS, which in case of OH include only the 163.13 μm line providing a lower limit for the ratio. Oxygen luminosities corrected for absorption are shown as light blue lines.

ence of the dense gas in the western outflow lobe, concentrated most strongly in the interaction region (Skretas et al. 2023). Accounting for the compression factor of at least 10, the gas densities from shock models are consistent with those obtained from radiative-transfer modeling of several transitions of CO and its rare isotopologues (Jakob et al. 2007). The observed single transition of the OH 163.13 μm line provides only a lower limit on the total OH luminosity from the source. We do not extrapolate the fluxes of other far-IR OH lines, because in high-mass protostars those lines are often detected in absorption and do not contribute to the gas cooling (Wampfler et al. 2013; Karska et al. 2014a). We conclude that the UV-irradiated C-shock models are consistent with the measured OH luminosities.

The assumed model shock velocities are within the range of line widths of velocity-resolved ^{13}CO 10-9 and H_2O profiles of ~ 15 km s^{-1} and ~ 24 km s^{-1} , respectively (van der Tak et al.

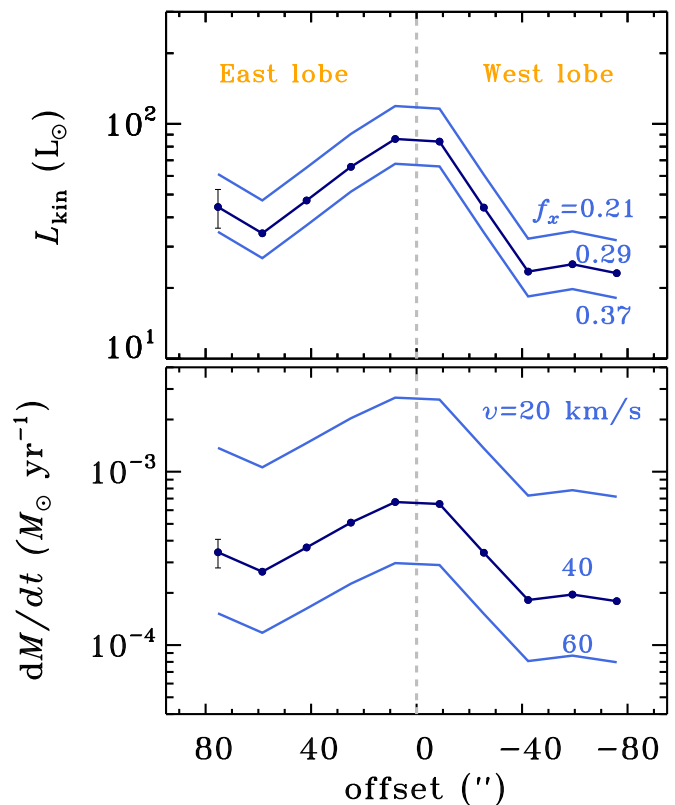


Fig. 16: Outflow power (top) and mass outflow rates (bottom) along the DR21 Main outflow. The vertical navy blue line shows a typical errorbar for observations assuming 20% calibration error (see Table 6). Light blue lines show a range of outflow power assuming a fraction of cooling, f_x , of 0.21 and 0.37 (top), and a range of mass loss rates assuming various shock velocities, v , of 20 and 60 km s^{-1} (bottom).

2010). The [O I] 63.18 μm profiles show blue wing emission up to ~ 40 km s^{-1} (Section 3), confirming the association of the atomic emission with outflow shocks. These velocities are likely lower limits of the actual gas velocities, since the DR21 Main outflow is close to the plane of the sky (Skretas et al. 2023). On the other hand, UV-irradiated shock models become fully dissociative already at ~ 30 km s^{-1} for G_0 of 0.1 and ~ 20 km s^{-1} for G_0 of 10 (Karska et al. 2018). A detailed geometry of the outflows would need to be implemented to properly model molecular emission arising from the shocks, which is outside the scope of this paper.

To summarize, far-IR line emission from all key gas cooling species is consistent with the origin in UV-irradiated C-shocks propagating along the outflow of DR21 Main. The observed ratios depend more strongly on the gas density than the considered strengths of the UV fields. The impact of UV fields is needed, however, to account for the bright [O I] and OH emission, which is clearly detected in the outflow spots. UV photons produced in-situ by shocks and those from the central OB stars can provide the necessary level of UV radiation along the outflow.

5.2. Energetics of the DR21 Main outflow

Gas cooling in the far-IR offers a useful measure of mechanical luminosity (or outflow power) deposited by protostellar outflows (Maret et al. 2009; Karska et al. 2018). Since its early observa-

Table 7: The ratio of [O I] and CO in high-mass YSOs and their outflows

Object	D (kpc)	L_{bol} (L_{\odot})	Class	[O I]/CO		References
				total ^a	selected lines ^b	
Orion Peak 1	0.4	–	outflow	0.2	1.6	Goicoechea et al. (2015)
W3-IRS5	2.0	2.1×10^5	HMPO	0.4 ± 0.1	1.9	van der Tak et al. (2013), Karska et al. (2014a)
G5.89-0.39	1.3	4.1×10^4	UCH II	0.95 ± 0.45	3.8	van der Tak et al. (2013), Karska et al. (2014a)
NGC7538-I1	2.7	1.1×10^5	UCH II	6.1 ± 3.1	16	van der Tak et al. (2013), Karska et al. (2014a)
DR21 Main	1.5	2.0×10^5	UCH II	4.2 ± 2.1	19.1 ± 8.3	this work

Notes. References are provided for the L_{bol} and [O I]-to-CO ratio, respectively. ^(a) CO luminosity extrapolated from the observed transitions using the CO excitation temperature (see Section 4.3). ^(b) CO luminosity calculated based on the two transitions directly observed with FIFI-LS.

tions, DR21 Main has been considered to drive one of the most powerful outflows in the Milky Way (Garden et al. 1986, 1990), and it is therefore vital to confront those estimates with FIFI-LS data.

Here, we use the total far-IR line cooling from the DR21 Main outflow to estimate the outflow power, L_{kin} , of DR21 Main based on Equation 2 from Maret et al. (2009):

$$L_{\text{kin}} = \frac{1}{2} \dot{M} v^2 = \frac{(1 - f_m)}{f_x} L_{\text{FIR}} \quad (5)$$

where f_m refers to the fraction of shock mechanical energy translated into excitation; f_x is the fraction of cooling due to far-IR emission of CO, [O I], [C II], and OH, namely L_{FIR} . The mass outflow rate, \dot{M} , can be conveniently calculated using Eq. 6:

$$\dot{M} = 1.24 \times 10^{-2} \frac{(1 - f_m)}{f_x} \left(\frac{L_{\text{FIR}}}{L_{\odot}} \right) \left(\frac{v}{\text{km/s}} \right)^{-2} M_{\odot}/\text{yr} \quad (6)$$

We adopt the value of f_m of 0.25 following Maret et al. (2009) and estimate f_x using our measurements and the literature data (see below). The H_2 luminosity from the entire outflow is $450 L_{\odot}$, when scaling the values reported in Garden et al. (1986) to the new distance of 1.5 kpc (Rygl et al. 2012). The H_2O luminosity can be estimated using the *Herschel*/SPIRE data; however, White et al. (2010) reported only the fluxes at the central part of DR21 Main. Therefore, we use archival data to obtain the line fluxes of H_2O using the data reduction and analysis techniques described in detail in Yang et al. (2018).

The H_2O line luminosity of DR21 Main covering lines detected in the SPIRE range equals $5.0 \times 10^{-3} L_{\odot}$, but this value constitutes only a small fraction of the total H_2O luminosity. The ratio of H_2O line luminosity, for lines detected in the PACS and SPIRE bands, ranges from a few to ~ 200 for low-mass protostars due to the differences in excitation (Karska et al. 2018; Yang et al. 2018). Adopting a median value of 14, the total estimated H_2O luminosity of DR21 Main is $7.0 \times 10^{-2} L_{\odot}$. Adopting the value of L_{FIR} calculated using absorption-corrected [O I] (Section 4.3), the fraction contributed to cooling from CO, OH, [O I] i.e. f_x , equals 0.29. If we do not correct for the presence of absorption in the atomic/ionic lines, we obtain f_x of 0.21.

Thus, for the entire DR21 Main outflow, we obtain the outflow power of $4.3\text{--}4.8 \times 10^2 L_{\odot}$, with the higher value corresponding to the absorption-corrected luminosities of the [O I] $63.18 \mu\text{m}$ and [C II] lines. The corresponding mass loss rates are in the range of $3.3\text{--}3.7 \times 10^{-3} M_{\odot} \text{yr}^{-1}$, assuming a velocity of 40 km s^{-1} . For shock velocities of 20 and 60 km s^{-1} , the corresponding mass loss rates are $1.3\text{--}1.5 \times 10^{-2}$ and $1.5\text{--}1.6 \times 10^{-3} M_{\odot} \text{yr}^{-1}$, respectively.

Skretas et al. (2023) calculated outflow parameters of the DR21 Main outflow from the HCO^+ 1-0 map obtained as part of the Cygnus Allscale Survey of Chemistry and Dynamical Environments (CASCADE, Beuther et al. 2022b). The outflow power of $2.4 \times 10^3 L_{\odot}$ is a factor of 5.0–5.6 higher than estimated here using Eq. 5, suggesting that the contribution of H_2O and OH cooling might be higher than assumed. The mass loss rate of $3.6 \times 10^{-2} M_{\odot} \text{yr}^{-1}$ from Skretas et al. (2023) is consistent with the results obtained here assuming shock velocities of 40 km s^{-1} . Compared to other high-mass protostars as discussed in Skretas et al. (2023), the slightly lower outflow powers found here are still in excess of $100 L_{\odot}$, confirming the status of DR21 Main as the most energetic outflow in the Milky Way.

5.3. Comparison of DR21 Main far-IR line cooling to other high-mass YSOs

The contribution of high- J CO lines to the total far-IR line cooling is $\sim 10\text{--}20\%$ in DR21 Main (see Section 4.3) – significantly lower than in other high-mass protostars observed with *Herschel*/PACS, characterized by a median $L_{\text{CO}}^{\text{tot}}$ of 74% (Karska et al. 2014a). This discrepancy cannot be assigned merely to the lack of H_2O lines observed with FIFI-LS, which were included in the definition of L_{FIR} adopted in earlier works (Nisini et al. 2002; Karska et al. 2014a). In contrast to water-rich low-mass protostars, a contribution of H_2O to L_{FIR} in high-mass objects ranges from only ~ 5 to 30% (Karska et al. 2014a, 2018), and is even lower toward Orion Peak 1, where all H_2O lines were detected in emission (Goicoechea et al. 2015). Thus, the differences between low- and high-mass protostars when it comes to the far-IR line cooling are evident (van Dishoeck et al. 2021).

Concerning the total CO emission, the differences between DR21 Main and other high-mass protostars might be twofold: (i) PACS measured multiple transitions of CO lines, whereas we extrapolate missing flux using only two lines observed by FIFI-LS (see Section 4.3); (ii) PACS measurements typically covered the central regions of $\sim 10^4$ AU of high-mass protostars (Karska et al. 2014a; Goicoechea et al. 2015), while the FIFI-LS map of DR21 Main covers spatial scales of $\sim 10^5$ AU (Section 1). The [O I] line cooling, on the other hand, can be heavily affected by absorption in the unresolved PACS or FIFI-LS spectra, which are well-seen in higher-resolution observations (see Fig. 6). The $63.18 \mu\text{m}$ line was detected in emission only toward 3 out of 10 PACS targets, where only the $145.53 \mu\text{m}$ line contributed to the oxygen line cooling (Karska et al. 2014a).

To compare the far-IR luminosities of high-mass protostars, we use the luminosity ratio of the [O I] and CO lines, which are either measured or easily extrapolated using FIFI-LS data. The

calculation of the luminosity of the [O I] 63.18 μm line toward DR21 Main accounts for the decrease of a factor of ~ 1.8 in the FIFI-LS flux due to absorption (Section 3.2). A similar factor, ~ 1.5 , was obtained by Leurini et al. (2015) toward G5.89-0.39 using GREAT data. Nonetheless, the physical extent of absorbing material versus the beam size might affect the measured [O I]-to-CO ratios and differ significantly between sources.

Table 7 shows the [O I]-to-CO ratio for a few high-mass protostars with a range of evolutionary stages, recently observed with *Herschel* and/or SOFIA. Both W3-IRS5 and G5.89-0.39 are characterized by rich H₂O and high- J CO emission, indicating the presence of recently shocked gas in the outflows (Karska et al. 2014a). In addition, G5.89-0.39 is a candidate explosive outflow source (Zapata et al. 2017), similar to DR21 Main, and has also developed a central H II region. NGC7538-IRS1 is probably the most evolved source in this sample, classified as the Ultra-Compact H II region (van der Tak et al. 2013).

We find that the [O I]-to-CO ratio is similar for NGC7538-IRS1 and DR21 Main, and consistently lower for the less evolved sources (Orion Peak 1, W3-IRS5, and G5.89-0.39). For sources where high-resolution observations are not available, a possible factor of 1.5-2 increase of the [O I] would not strongly affect the trend.

The [O I]-to-CO could increase for more massive sources (Lê et al. 2023), but the sources considered here all have similar bolometric luminosities. Thus, there is likely an evolutionary trend in high-mass protostars reflected in the cooling channels of the gas in the far-IR. However, a significantly larger sample of sources with high-spectral resolution observations would be necessary to solidify our conclusion.

6. Conclusions

We have characterized the SOFIA/FIFI maps of DR21 Main and identified its substructures dominated by molecular, atomic, and ionized gas. We have quantified the far-IR line emission along the outflow and linked it with variations in the gas physical conditions. The conclusions are the following.

1. Emission in the high- J CO, [O I] 63.18 μm , and OH lines follows the DR21 Main outflow direction obtained from the H₂ $v=1-0$ S(1) and HCO⁺ 1-0 observations. In contrast, emission in the [C II] and [O I] 145.53 μm is localized mainly in the eastern outflow lobe, and does not extend to the interaction region in the western outflow lobe. Emission in the [O III] lines pinpoints an extended cavity of ionized gas in the eastern outflow lobe, associated with the cometary tail of the H II region.
2. Excitation temperatures in the range from ~ 170 to 360 K are determined using the ratio of CO 14-13 and 16-15 lines assuming LTE. The highest temperatures are characteristic for the interaction region in the western outflow lobe, where several high-density tracers have been identified using the CASCADE survey (Skretas et al. 2023). H₂ densities above 10^5 cm^{-3} are necessary to reproduce the observed CO line ratios in the obtained temperature range along the outflow using non-LTE radiative-transfer models.
3. Physical conditions of atomic gas are obtained from the non-LTE radiative transfer models and the observed ratios of [O I] lines, once the fluxes of the 63.18 μm line are corrected for unresolved absorption using data from GREAT. Atomic hydrogen densities from 10^4 to 10^5 cm^{-3} and molecular hydrogen densities from 10^4 to $10^{5.5} \text{ cm}^{-3}$ are obtained in the limit where both fine-structure lines are optically thin (N of 10^{17}

cm^{-2} , $dv=40 \text{ km s}^{-1}$), for the temperature range from 300 to 1000 K. For oxygen column densities of 10^{19} cm^{-2} , the 63.18 μm line becomes optically thick at low densities, but the highest values of the observed ratio are well-reproduced by H₂ densities below 10^6 cm^{-3} and H densities below 10^5 cm^{-3} .

4. Average electron densities of 240-280 cm^{-3} are determined for the central H II regions using two [O III] lines. Somewhat higher densities, up to 410 cm^{-3} , are measured when considering smaller areas on the sky along the outflow.
5. The bulk of high- J CO and [O I] 63.18 μm emission likely arises in the UV-irradiated non-dissociative shocks with G_0 of 0.1 to 10 times the interstellar radiation field. The ratio of [O I] over CO luminosity is higher in the eastern lobe, consistent with lower H₂ densities from shock models. On the contrary, the lower ratio is consistent with higher pre-shock densities in the western outflow lobe, consistent with the presence of the interaction region.
6. [O I] is a major coolant among the far-IR lines observed by FIFI-LS and accounts for at least 62 to 76% of the total far-IR gas cooling, L_{tot} . CO is another important coolant with contributions of 8 to 27 % to L_{tot} , whereas [C II] accounts for 9 to 20 % of far-IR line cooling. The relatively low fraction of molecular cooling of DR21 Main might be linked with the advanced evolutionary stage of the region.
7. The power of the DR21 Main outflow calculated from the total far-IR cooling of $4.3 - 4.8 \times 10^2 L_{\odot}$ is consistent within a factor of 5 with previous measurements using HCO⁺ 1-0, and places the source among the most energetic of the known outflows in the Milky Way. The mass outflow rates in excess of $3.3 - 3.7 \times 10^{-3} M_{\odot} \text{ yr}^{-1}$ confirm a significant mass of currently-shocked gas along the outflow, in particular in its western outflow lobe.

FIFI-LS data offers sufficient angular resolution to disentangle the structure of DR21 Main outflow, and allows for robust comparisons of multiple gas cooling species with shock models. Observations of much less extended outflows and/or those at larger distances are currently possible mainly using the key gas coolant – H₂ – using the James Webb Space Telescope.

Acknowledgements. The authors would like to thank the anonymous referee for the comments that helped to improve this manuscript. The authors also thank Volker Ossenkopf for useful discussions concerning the parallel analysis of the GREAT observations of DR21. AK and MF acknowledge support from the Polish National Agency for Academic Exchange grants No. BPN/BEK/2021/1/00319/DEC/1 and BPN/BEK/2023/1/00036/DEC/01, respectively. MF acknowledges also support from the Polish National Science Centre via the grant UMO-2022/47/D/ST9/00419. Y.-L.Y. acknowledges support from Grant-in-Aid from the Ministry of Education, Culture, Sports, Science, and Technology of Japan (20H05845, 20H05844, 22K20389), and a pioneering project in RIKEN (Evolution of Matter in the Universe). Based on observations made with the NASA/DLR Stratospheric Observatory for Infrared Astronomy (SOFIA). SOFIA is jointly operated by the Universities Space Research Association, Inc. (USRA), under NASA contract NAS2-97001, and the Deutsches SOFIA Institut (DSI) under DLR contract 50 OK 0901 to the University of Stuttgart. GREAT is a development by the MPI für Radioastronomie and the KOSMA/Universität zu Köln, in cooperation with the DLR Institut für Optische Sensorsysteme, financed by the participating institutes, by the German Aerospace Center (DLR) under grants 50 OK 1102, 1103 and 1104, and within the Collaborative Research Centre 956, funded by the Deutsche Forschungsgemeinschaft (DFG). *Herschel* was an ESA space observatory with science instruments provided by European-led Principal Investigator consortia and with important participation from NASA.

References

- Ashby, M. L. N., Bergin, E. A., Plume, R., et al. 2000, *ApJ*, 539, L115
Bally, J. 2016, *ARA&A*, 54, 491

- Beck, A., Lebouteiller, V., Madden, S. C., et al. 2022, *A&A*, 665, A85
- Benz, A. O., Bruderer, S., van Dishoeck, E. F., et al. 2016, *A&A*, 590, A105
- Bergin, E. A., Neufeld, D. A., & Melnick, G. J. 1998, *ApJ*, 499, 777
- Bernard, A., Neichel, B., Samal, M. R., et al. 2016, *A&A*, 592, A77
- Bertin, E., Mellier, Y., Radovich, M., et al. 2002, in *Astronomical Society of the Pacific Conference Series*, Vol. 281, *Astronomical Data Analysis Software and Systems XI*, ed. D. A. Bohlender, D. Durand, & T. H. Handley, 228
- Beuther, H., Schneider, N., Simon, R., et al. 2022a, *A&A*, 659, A77
- Beuther, H., Wyrowski, F., Menten, K. M., et al. 2022b, *A&A*, 665, A63
- Bonne, L., Bontemps, S., Schneider, N., et al. 2023a, *ApJ*, 951, 39
- Bonne, L., Kabanovic, S., Schneider, N., et al. 2023b, *A&A*, 679, L5
- Bonne, L., Schneider, N., García, P., et al. 2022, *ApJ*, 935, 171
- Bontemps, S., Motte, F., Csengeri, T., & Schneider, N. 2010, *A&A*, 524, A18
- Bruderer, S., Benz, A. O., Doty, S. D., van Dishoeck, E. F., & Bourke, T. L. 2009, *ApJ*, 700, 872
- Brunthaler, A., Menten, K. M., Dzib, S. A., et al. 2021, *A&A*, 651, A85
- Cao, Y., Qiu, K., Zhang, Q., et al. 2019, *ApJS*, 241, 1
- Caratti o Garatti, A., Ray, T. P., Kavanagh, P. J., et al. 2024, *A&A*, 691, A134
- Ceccarelli, C., Hollenbach, D. J., & Tielens, A. G. G. M. 1996, *ApJ*, 471, 400
- Cesaroni, R., Faustini, F., Galli, D., et al. 2023, *A&A*, 671, A126
- Clegg, P. E., Ade, P. A. R., Armand, C., et al. 1996, *A&A*, 315, L38
- Cruz-González, I., Salas, L., & Hiriart, D. 2007, *Rev. Mexicana Astron. Astrofis.*, 43, 337
- Csengeri, T., Wyrowski, F., Menten, K. M., et al. 2022, *A&A*, 658, A193
- Cyganowski, C. J., Reid, M. J., Fish, V. L., & Ho, P. T. P. 2003, *ApJ*, 596, 344
- Dale, J. E., Haworth, T. J., & Bressert, E. 2015, *MNRAS*, 450, 1199
- Davis, C. J., Kumar, M. S. N., Sandell, G., et al. 2007, *MNRAS*, 374, 29
- de Graauw, T., Helmich, F. P., Phillips, T. G., et al. 2010, *A&A*, 518, L6
- Deharveng, L., Zavagno, A., & Caplan, J. 2005, *A&A*, 433, 565
- Dickel, J. R., Dickel, H. R., & Wilson, W. J. 1978, *ApJ*, 223, 840
- Doty, S. D. & Neufeld, D. A. 1997, *ApJ*, 489, 122
- Fischer, C., Beckmann, S., Bryant, A., et al. 2018, *Journal of Astronomical Instrumentation*, 7, 1840003
- Fischer, C., Iserlohe, C., Vacca, W., et al. 2021, *PASP*, 133, 055001
- Flower, D. R. & Pineau Des Forêts, G. 2010, *MNRAS*, 406, 1745
- Garden, R., Geballe, T. R., Gatley, I., & Nadeau, D. 1986, *MNRAS*, 220, 203
- Garden, R. P., Hayashi, M., Gatley, I., Hasegawa, T., & Kaifu, N. 1991, *ApJ*, 374, 540
- Garden, R. P., Russell, A. P. G., & Burton, M. G. 1990, *ApJ*, 354, 232
- Geen, S., Bieri, R., Rosdahl, J., & de Koter, A. 2021, *MNRAS*, 501, 1352
- Geen, S., Pellegrini, E., Bieri, R., & Klessen, R. 2020, *MNRAS*, 492, 915
- Genzel, R. & Downes, D. 1977, *A&AS*, 30, 145
- Godard, B., Pineau des Forêts, G., Lesaffre, P., et al. 2019, *A&A*, 622, A100
- Goicoechea, J. R., Chavarría, L., Cernicharo, J., et al. 2015, *ApJ*, 799, 102
- Goldsmith, P. F. 2019, *ApJ*, 887, 54
- Goldsmith, P. F. & Langer, W. D. 1978, *ApJ*, 222, 881
- Goldsmith, P. F., Langer, W. D., Pineda, J. L., & Velusamy, T. 2012, *ApJS*, 203, 13
- Green, J. D., Evans, Neal J., I., Jørgensen, J. K., et al. 2013, *ApJ*, 770, 123
- Green, J. D., Yang, Y.-L., Evans, Neal J., I., et al. 2016, *AJ*, 151, 75
- Griffin, M. J., Abergel, A., Abreu, A., et al. 2010, *A&A*, 518, L3
- Gusdorf, A., Güsten, R., Menten, K. M., et al. 2016, *A&A*, 585, A45
- Guzmán Ccolque, E., Fernández López, M., Zapata, L. A., Bally, J., & Rivera-Ortiz, P. R. 2024, *A&A*, 689, A339
- Habing, H. J. 1968, *Bull. Astron. Inst. Netherlands*, 19, 421
- Harris, S. 1973, *MNRAS*, 162, 5P
- Herczeg, G. J., Karska, A., Bruderer, S., et al. 2012, *A&A*, 540, A84
- Herpin, F., Chavarría, L., Jacq, T., et al. 2016, *A&A*, 587, A139
- Herpin, F., Chavarría, L., van der Tak, F., et al. 2012, *A&A*, 542, A76
- Heyminck, S., Graf, U. U., Güsten, R., et al. 2012, *A&A*, 542, L1
- Hoang, T. D., Karska, A., Lee, M. Y., et al. 2023, *A&A*, 679, A121
- Hollenbach, D., Elitzur, M., & McKee, C. F. 2013, *ApJ*, 773, 70
- Hollenbach, D. & McKee, C. F. 1989, *ApJ*, 342, 306
- Iserlohe, C., Fischer, C., Vacca, W. D., et al. 2021, *PASP*, 133, 055002
- Jacq, T., Braine, J., Herpin, F., van der Tak, F., & Wyrowski, F. 2016, *A&A*, 595, A66
- Jakob, H., Kramer, C., Simon, R., et al. 2007, *A&A*, 461, 999
- Karska, A., Herczeg, G. J., van Dishoeck, E. F., et al. 2013, *A&A*, 552, A141
- Karska, A., Herpin, F., Bruderer, S., et al. 2014a, *A&A*, 562, A45
- Karska, A., Kaufman, M. J., Kristensen, L. E., et al. 2018, *ApJS*, 235, 30
- Karska, A., Kristensen, L. E., van Dishoeck, E. F., et al. 2014b, *A&A*, 572, A9
- Kaufman, M. J. & Neufeld, D. A. 1996, *ApJ*, 456, 611
- Kaufman, M. J., Wolfire, M. G., Hollenbach, D. J., & Luhman, M. L. 1999, *ApJ*, 527, 795
- Kessler, M. F., Steinz, J. A., Anderegg, M. E., et al. 1996, *A&A*, 315, L27
- Khan, S., Rugel, M. R., Brunthaler, A., et al. 2024, *A&A*, 689, A81
- Klein, B., Hochgürtel, S., Krämer, I., et al. 2012, *A&A*, 542, L3
- Klein, R., Beckmann, S., Bryant, A., et al. 2014, in *Society of Photo-Optical Instrumentation Engineers (SPIE) Conference Series*, Vol. 9147, *Ground-based and Airborne Instrumentation for Astronomy V*, ed. S. K. Ramsay, I. S. McLean, & H. Takami, 91472X
- Kristensen, L. E., van Dishoeck, E. F., Benz, A. O., et al. 2013, *A&A*, 557, A23
- Kristensen, L. E., van Dishoeck, E. F., Bergin, E. A., et al. 2012, *A&A*, 542, A8
- Kristensen, L. E., van Dishoeck, E. F., Mottram, J. C., et al. 2017, *A&A*, 605, A93
- Krumholz, M. R., Bate, M. R., Arce, H. G., et al. 2014, *Protostars and Planets VI*, 243
- Lane, A. P., Haas, M. R., Hollenbach, D. J., & Erickson, E. F. 1990, *ApJ*, 361, 132
- Lê, N., Karska, A., Figueira, M., et al. 2023, *A&A*, 674, A64
- Leurini, S., Herpin, F., van der Tak, F., et al. 2017, *A&A*, 602, A70
- Leurini, S., Wyrowski, F., Wiesemeyer, H., et al. 2015, *A&A*, 584, A70
- Lique, F., Klos, J., Alexander, M. H., Le Picard, S. D., & Dalgarno, P. J. 2018, *MNRAS*, 474, 2313
- Liseau, R., Justtanont, K., & Tielens, A. G. G. M. 2006, *A&A*, 446, 561
- Luisi, M., Anderson, L. D., Schneider, N., et al. 2021, *Science Advances*, 7, eabe9511
- Luridiana, V., Morisset, C., & Shaw, R. A. 2015, *A&A*, 573, A42
- Manoj, P., Watson, D. M., Neufeld, D. A., et al. 2013, *ApJ*, 763, 83
- Maret, S., Bergin, E. A., Neufeld, D. A., et al. 2009, *ApJ*, 698, 1244
- Marston, A. P., Reach, W. T., Noriega-Crespo, A., et al. 2004, *ApJS*, 154, 333
- Martins, F., Schaefer, D., & Hillier, D. J. 2005, *A&A*, 436, 1049
- Melnick, G. J. & Kaufman, M. J. 2015, *ApJ*, 806, 227
- Moore, C. E. 1985, *Selected tables of atomic spectra. Atomic energy levels and multiplet table O3*
- Motte, F., Bontemps, S., & Louvet, F. 2018, *ARA&A*, 56, 41
- Motte, F., Bontemps, S., Schilke, P., et al. 2007, *A&A*, 476, 1243
- Mottram, J. C., Kristensen, L. E., van Dishoeck, E. F., et al. 2014, *A&A*, 572, A21
- Mottram, J. C., van Dishoeck, E. F., Kristensen, L. E., et al. 2017, *A&A*, 600, A99
- Neufeld, D. A. 2012, *ApJ*, 749, 125
- Neufeld, D. A. & Dalgarno, A. 1989, *ApJ*, 340, 869
- Neufeld, D. A., Manoj, P., Tyagi, H., et al. 2024, *ApJ*, 966, L22
- Nisini, B., Giannini, T., & Lorenzetti, D. 2002, *ApJ*, 574, 246
- Nisini, B., Santangelo, G., Giannini, T., et al. 2015, *ApJ*, 801, 121
- Oliveira, J. M., van Loon, J. T., Sewilo, M., et al. 2019, *MNRAS*, 490, 3909
- Ossenkopf, V., Koumpia, E., Okada, Y., et al. 2015, *A&A*, 580, A83
- Ossenkopf, V., Röllig, M., Simon, R., et al. 2010, *A&A*, 518, L79
- Peters, T., Klaassen, P. D., Mac Low, M.-M., et al. 2014, *ApJ*, 788, 14
- Pickett, H. M., Poynter, R. L., Cohen, E. A., et al. 1998, *J. Quant. Spectr. Rad. Transf.*, 60, 883
- Pilbratt, G. L., Riedinger, J. R., Passvogel, T., et al. 2010, *A&A*, 518, L1
- Plambeck, R. L. & Menten, K. M. 1990, *ApJ*, 364, 555
- Poglitsch, A., Herrmann, F., Genzel, R., et al. 1996, *ApJ*, 462, L43
- Poglitsch, A., Waelkens, C., Geis, N., et al. 2010, *A&A*, 518, L2
- Risacher, C., Güsten, R., Stutzki, J., et al. 2018, *Journal of Astronomical Instrumentation*, 7, 1840014
- Roelfsema, P. R., Goss, W. M., & Geballe, T. R. 1989, *A&A*, 222, 247
- Russell, A. P. G., Bally, J., Padman, R., & Hills, R. E. 1992, *ApJ*, 387, 219
- Rygl, K. L. J., Brunthaler, A., Sanna, A., et al. 2012, *A&A*, 539, A79
- San José-García, I., Mottram, J. C., Kristensen, L. E., et al. 2013, *A&A*, 553, A125
- San José-García, I., Mottram, J. C., van Dishoeck, E. F., et al. 2016, *A&A*, 585, A103
- Schneider, N., Bonne, L., Bontemps, S., et al. 2023, *Nature Astronomy*, 7, 546
- Schneider, N., Bontemps, S., Motte, F., et al. 2016, *A&A*, 591, A40
- Schneider, N., Bontemps, S., Simon, R., et al. 2006, *A&A*, 458, 855
- Schneider, N., Csengeri, T., Bontemps, S., et al. 2010, *A&A*, 520, A49
- Schneider, N., Röllig, M., Simon, R., et al. 2018, *A&A*, 617, A45
- Schneider, N., Simon, R., Guevara, C., et al. 2020, *PASP*, 132, 104301
- Schöier, F. L., van der Tak, F. F. S., van Dishoeck, E. F., & Black, J. H. 2005, *A&A*, 432, 369
- Skretas, I. M., Karska, A., Wyrowski, F., et al. 2023, *A&A*, 679, A66
- Smith, M. D., Davis, C. J., Rowles, J. H., & Knight, M. 2014, *MNRAS*, 443, 2612
- Smith, M. D., Eisloffel, J., & Davis, C. J. 1998, *MNRAS*, 297, 687
- Sperling, T., Eisloffel, J., Fischer, C., et al. 2021, *A&A*, 650, A173
- Tielens, A. G. G. M. & Hollenbach, D. 1985, *ApJ*, 291, 722
- Tiwari, M., Wolfire, M., Pound, M. W., et al. 2022, *AJ*, 164, 150
- Tychoniec, Ł., van Gelder, M. L., van Dishoeck, E. F., et al. 2024, *A&A*, 687, A36
- van der Tak, F. F. S., Black, J. H., Schöier, F. L., Jansen, D. J., & van Dishoeck, E. F. 2007, *A&A*, 468, 627
- van der Tak, F. F. S., Chavarría, L., Herpin, F., et al. 2013, *A&A*, 554, A83
- van der Tak, F. F. S., Marseille, M. G., Herpin, F., et al. 2010, *A&A*, 518, L107
- van der Tak, F. F. S., Shipman, R. F., Jacq, T., et al. 2019, *A&A*, 625, A103

- van Dishoeck, E. F., Kristensen, L. E., Mottram, J. C., et al. 2021, *A&A*, 648, A24
- van Gelder, M. L., Francis, L., van Dishoeck, E. F., et al. 2024, *A&A*, 692, A197
- van Kempen, T. A., Kristensen, L. E., Herczeg, G. J., et al. 2010, *A&A*, 518, L121
- van Kempen, T. A., van Dishoeck, E. F., Güsten, R., et al. 2009, *A&A*, 501, 633
- Visser, R., Kristensen, L. E., Bruderer, S., et al. 2012, *A&A*, 537, A55
- Wampfler, S. F., Bruderer, S., Karska, A., et al. 2013, *A&A*, 552, A56
- Wampfler, S. F., Bruderer, S., Kristensen, L. E., et al. 2011, *A&A*, 531, L16
- White, G. J., Abergel, A., Spencer, L., et al. 2010, *A&A*, 518, L114
- Yang, B., Stancil, P. C., Balakrishnan, N., & Forrey, R. C. 2010, *ApJ*, 718, 1062
- Yang, Y.-L., Evans, N. J., Karska, A., et al. 2022, *ApJ*, 925, 93
- Yang, Y.-L., Green, J. D., Evans, Neal J., I., et al. 2018, *ApJ*, 860, 174
- Yıldız, U. A., Kristensen, L. E., van Dishoeck, E. F., et al. 2015, *A&A*, 576, A109
- Young, E. T., Becklin, E. E., Marcum, P. M., et al. 2012, *ApJ*, 749, L17
- Zapata, L. A., Schmid-Burgk, J., Pérez-Goytia, N., et al. 2013, *ApJ*, 765, L29
- Zapata, L. A., Schmid-Burgk, J., Rodríguez, L. F., Palau, A., & Loinard, L. 2017, *ApJ*, 836, 133

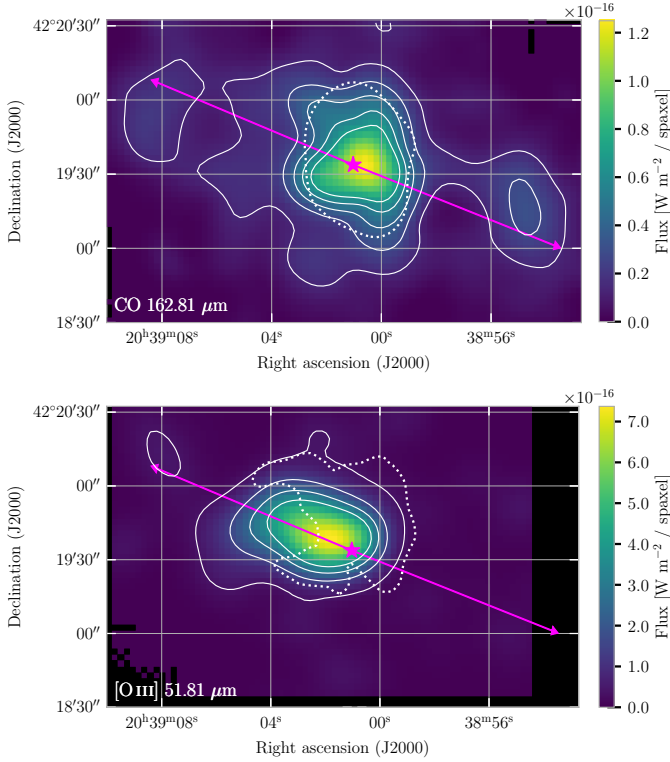
Appendix A: Additional FIFI-LS maps of DR21 Main


Fig. A.1: Integrated intensity maps of the CO 16-15 line at $162.81 \mu\text{m}$ (top) and the $[\text{O III}]$ line at $51.81 \mu\text{m}$ (bottom). Solid contours show the line emission in steps of 5σ , 10σ , 15σ , 20σ , 25σ (top) and 5σ , 20σ , 35σ , 50σ (bottom). Dotted contours show the extent of the continuum emission in the close vicinity of the targeted lines at the 5σ level. See also Figures 2 and 3.

In this Appendix, we show maps of DR21 Main outflow in additional far-IR lines observed with FIFI-LS (see Table A.1), which are qualitatively similar to the ones already presented in Section 3.1. We also present the maps of continuum emission from FIFI-LS and discuss the continuum peaks at far-IR.

Figure A.1 shows the integrated intensity map of DR21 Main in the CO 16-15 line at $162.81 \mu\text{m}$ and the $[\text{O III}]$ line at $51.81 \mu\text{m}$. The spatial extent of CO 16-15 emission resemble that of CO 14-13. The strongest peak is detected toward the center of DR21 Main, and weaker emission is found along the outflow direction including a clear peak in the interaction region (Skrutas et al. 2023). The $[\text{O III}]$ line peaks in the eastern outflow lobe of DR21 Main, following a cometary tail of the H II region. The extent of emission is similar to the $[\text{O III}]$ line at $88.35 \mu\text{m}$; however, it is offset from the $[\text{O I}]$ and $[\text{C II}]$ emission peaks tracing atomic gas (Fig. A.2, see also Section 3.1).

Figure A.3 compares the spatial extent of the two $[\text{O I}]$ lines, the $[\text{O I}]$ line at $145.53 \mu\text{m}$ and the $[\text{C II}]$ line, and the CO 14-13 and the $[\text{C II}]$ line. The $[\text{O I}]$ line at $63.18 \mu\text{m}$ closely follows the outflow direction in both outflow lobes, whereas the $[\text{O I}]$ line at $145.53 \mu\text{m}$ and the $[\text{C II}]$ line are detected mainly toward the eastern outflow lobe. The interaction region in the western outflow lobe is clearly detected both in the $[\text{O I}]$ line at $63.18 \mu\text{m}$ and the CO 14-13 line. For more discussion, see Section 3.1.

Figures A.4–A.5 show the spatial extent of continuum emission at the far-IR wavelengths observed with FIFI-LS at their

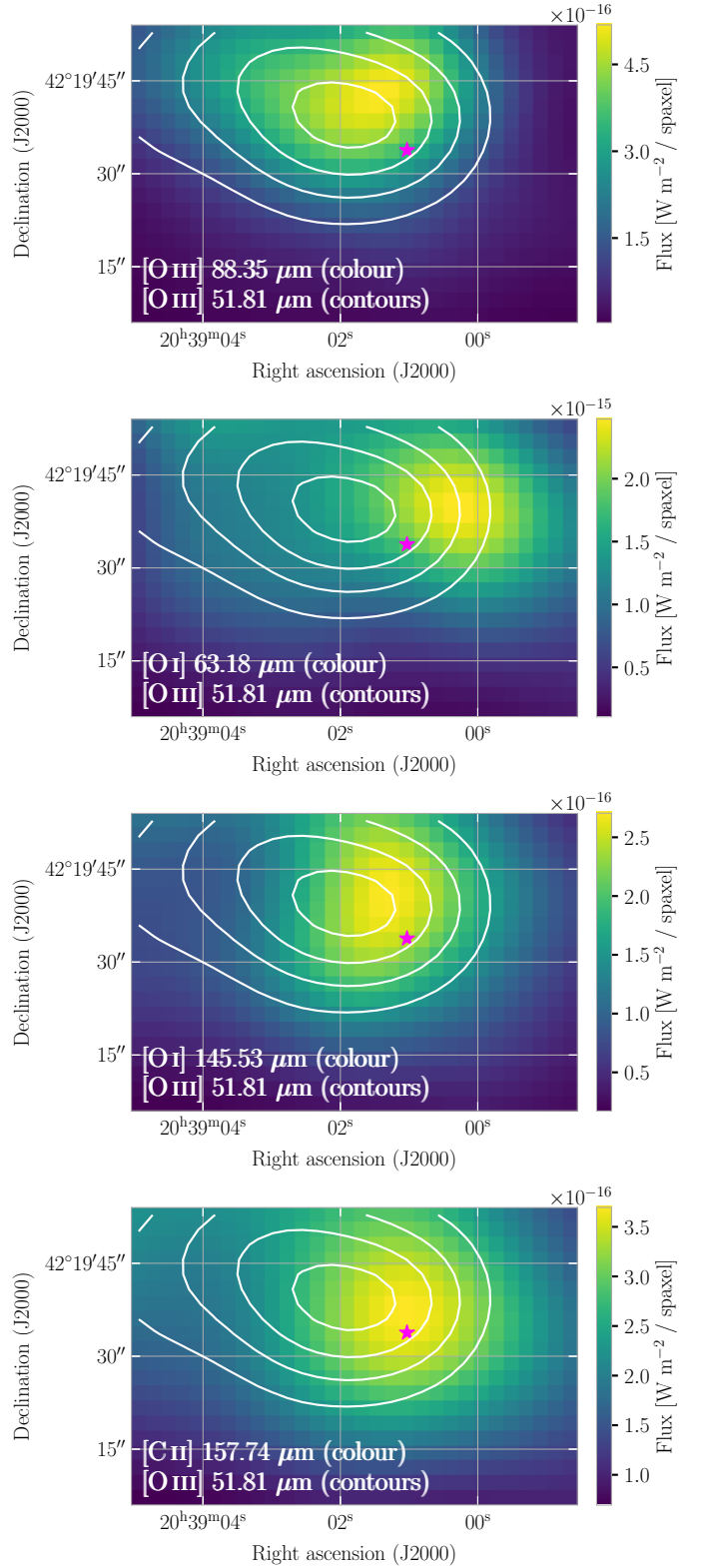


Fig. A.2: Integrated intensity maps of the $[\text{O III}]$ $51.81 \mu\text{m}$ (contours) and, from top to bottom, the $[\text{O III}]$ at $88.35 \mu\text{m}$, the $[\text{O I}]$ line at $63.18 \mu\text{m}$, the $[\text{O I}]$ line at $145.53 \mu\text{m}$, and the $[\text{C II}]$ at $157.74 \mu\text{m}$ (colors). Contours are drawn with the steps of 50σ , 90σ , 130σ and 170σ .

native angular resolution (see Table 1). The continuum values were calculated using emission-free regions of the spectra on

Table A.1: Summary of the SOFIA observations

Date	Instrument	Project ID	Mode	Lines observed
23/10/2015	FIFI-LS	87_0001	GTO	[O I] 63.18 μm , 145.53 μm , [C II]
10/06/2017	GREAT	04_0111	Cycle 4	[O I] 63.18 μm , CO 16-15, [C II]
13/11/2019	FIFI-LS	75_0046	DDT	[O III] 51.81 μm , CO 14-13
03/09/2020	FIFI-LS	75_0046	DDT	[O I] 145.53 μm , CO 16-15, OH
08/01/2022	FIFI-LS	09_0079	Cycle 9	[O III] 88.35 μm , CO 16-15, OH
13/01/2022	FIFI-LS	09_0079	Cycle 9	[O III] 51.82 μm , 88.35 μm , [O I] 145.53 μm , [C II]
14/01/2022	FIFI-LS	09_0079	Cycle 9	[O III] 51.82 μm , 88.35 μm , [O I] 145.53 μm [C II], CO 16-15, OH, CO 14-13
31/08/2022	FIFI-LS	09_0079	Cycle 9	[O III] 88.35 μm

both sides of the targeted lines. Subsequently, we used the `scipy` optimize package to obtain the central coordinates at each far-

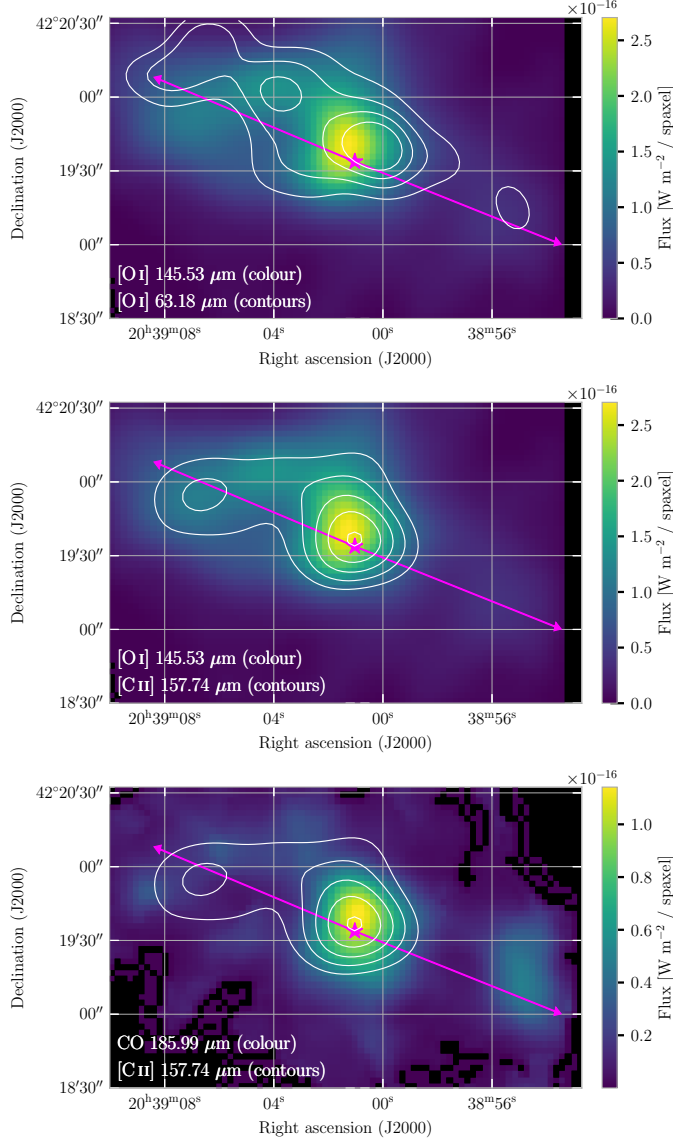


Fig. A.3: Integrated intensity maps of the [O I] 145.53 μm in colors and [O I] 63.18 μm in contours (35σ , 55σ , 75σ , 95σ ; top), [O I] 145.53 μm in colors and [C II] 157.74 μm in contours (9σ , 11σ , 13σ , 15σ , 17σ , middle), and CO 185.99 μm in colors and [C II] 157.74 μm in contours (bottom) toward DR21 Main with SOFIA FIFI-LS.

Table A.2: Positions of the far-IR continuum peaks toward DR21 Main

λ (μm)	α_{J2000}	δ_{J2000}	Separation DR21-1 ($''$)
51.81	20:39:00.49	+42:19:45.6	13.2
63.18	20:39:00.57	+42:19:44.1	11.5
88.35	20:39:00.77	+42:19:43.2	9.8
145.53	20:39:00.91	+42:19:39.2	5.6
157.74	20:39:00.72	+42:19:36.2	4.2
162.81	20:39:00.76	+42:19:37.4	4.6
185.99	20:39:00.75	+42:19:38.4	5.6

Table A.3: Continuum fluxes from SOFIA and ISO toward the center of DR21 Main in units of Jy

λ (μm)	$F_{\lambda}(\text{FIFI-LS})$ (10^3 Jy)	$F_{\lambda}(\text{ISO})$ (10^3 Jy)	Difference
51.81	10.88	16.11	-0.48
63.17	13.76	22.3	-0.62
88.35	18.28	24.06	-0.32
145.53	9.81	12.88	-0.31
157.74	10.7	11.04	-0.03
162.81	8.48	10.34	-0.22
185.99	7.18	7.74	-0.08

Notes. The difference in continuum emission is estimated as $1 - F_{\lambda}(\text{ISO})/F_{\lambda}(\text{FIFI-LS})$.

IR wavelength assuming a 2D Gaussian distribution of continuum emission. The resulting positions of the far-IR continuum peaks are shown on the continuum maps and in Table A.2, and compared with the coordinates of the DR21-1 core at $(\alpha, \delta)_{J2000} = (20^{\text{h}}39^{\text{m}}01^{\text{s}}03, +42^{\circ}19'33''.8)$ from Cao et al. (2019). There is an agreement, below the size of the FIFI-LS beam, between peak positions of the continuum above 100 μm and the coordinates of the DR21-1 core extracted from the far-IR to millimeter photometric maps (Cao et al. 2019). At wavelengths below 100 μm , however, the separation with respect to the DR21-1 core is larger than the beam size, indicating that the warmer dust peaks several arcseconds to the North.

A comparison of the far-IR continuum values between the FIFI-LS and ISO observations is shown in Table A.3. Here, we extracted the fluxes from the fit parameters of the single isothermal gray-body model, because the measurements were not reported in a tabular form (Jakob et al. 2007). The continuum values are in agreement within the 30% calibration error for most wavelengths. Larger differences are found at 52 and 63 μm wavelength ($\geq 50\%$), which might be due to the fixed solid angle in the model (too large for short λ), problems with discontinuities be-

tween channels of ISO (see Fig. 7 of Jakob et al. 2007), or true differences due to flux variability.

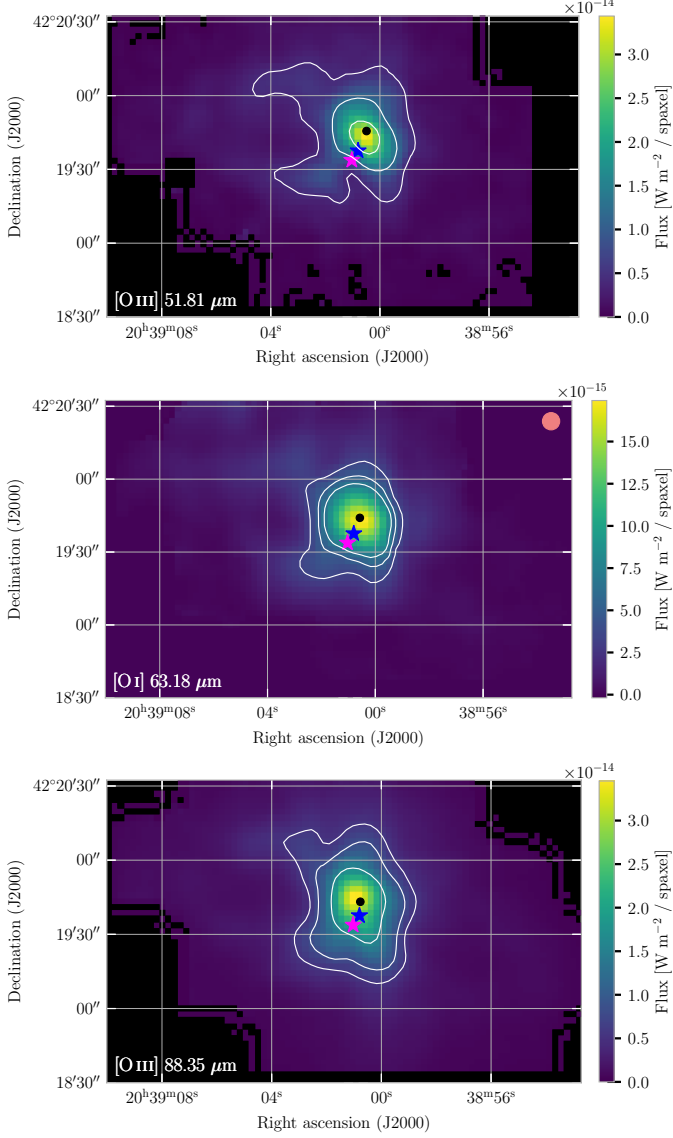


Fig. A.4: Continuum emission from FIFI-LS at wavelengths below $100 \mu\text{m}$. From top to bottom, the maps show the distribution of continuum emission with contours in the vicinity of the [O III] line at $51.81 \mu\text{m}$ (5 , 15 , and 30σ), [O I] line at $63.18 \mu\text{m}$ (10 , 15 , and 20σ), and [O III] line at $88.35 \mu\text{m}$ (10 , 15 , and 30σ). The magenta and blue stars show the center of DR21-1 core (Cao et al. 2019) and the center of the explosive outflow (Guzmán Ccolque et al. 2024). The black dot indicates the continuum center from 2D Gaussian fitting (see Tab. A.2), and the beam size is shown for the [O I] line at $63.18 \mu\text{m}$ as an orange circle.

Appendix B: Velocity-resolved profiles from SOFIA/GREAT

Unresolved absorption might affect the integrated line flux measured by FIFI-LS toward DR21 Main (Section 3.2). Here, we use archival observations from SOFIA/GREAT to estimate the total line fluxes of the [O I] $63.18 \mu\text{m}$ line, observed in common by the two instruments and the factor by which those fluxes are un-

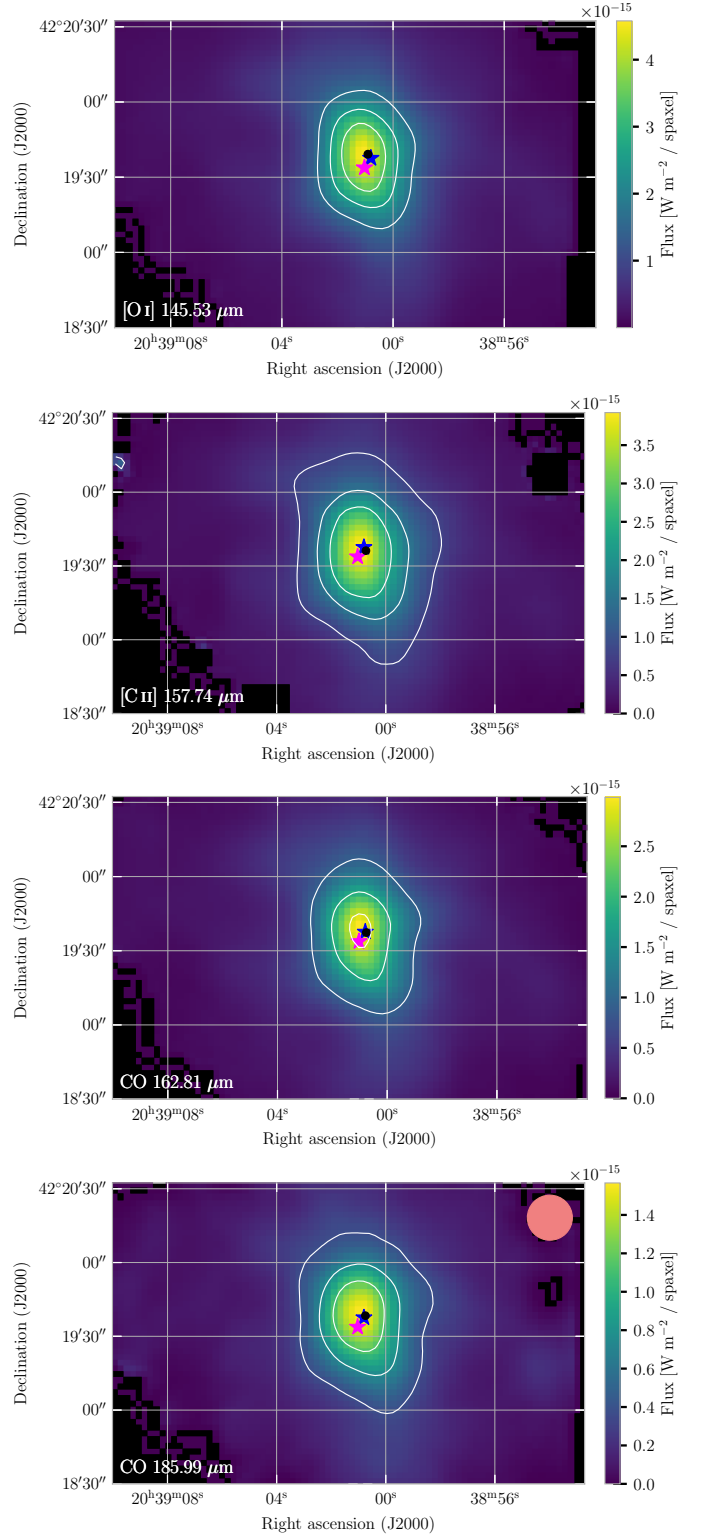


Fig. A.5: Continuum emission from FIFI-LS at wavelengths above $100 \mu\text{m}$. From top to bottom, the maps show the distribution of continuum emission with contours in the vicinity of the [O I] line at $145.53 \mu\text{m}$ (10 , 15 , 20σ), [C II] line at $157.74 \mu\text{m}$ (6 , 12 , 18σ), and CO 16-15 and 14-13 lines at 162.81 (10 , 20 , and 30σ) and $185.99 \mu\text{m}$ (5 , 10 , and 15σ) respectively. The beam size is shown for the CO 14-13 line at $185.99 \mu\text{m}$.

derestimated by FIFI-LS. For the comparison with FIFI-LS, the GREAT maps were convolved to the same resolution of $18.3''$.

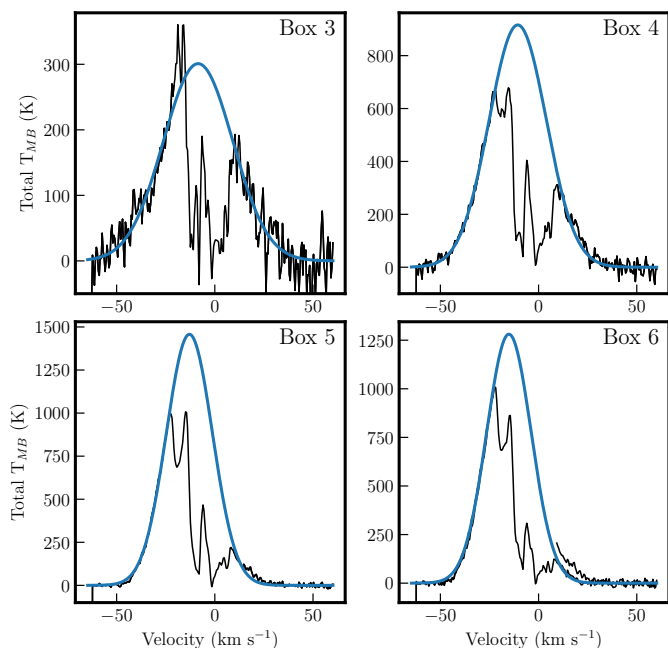


Fig. B.1: Spectra for [O I] 63.18 μm from GREAT (black). The part of the spectrum where absorption is observed is not taken into account for the Gaussian fitting (blue).

Figure B.1 shows the line profiles of the [O I] 63.18 μm from GREAT, which are used to recover the total flux of the line. To obtain the fit, we omit the parts of the profiles which are most strongly affected by absorption. Those features appear in similar locations in all profiles, in the vicinity of source velocity and possible components from the W75 complex. The fit is performed for boxes 3, 4, 5 and 6 (see Fig. B.2). We integrate both the spectra and the Gaussian fit of the spectra to obtain the luminosity in each box.

The resulting line luminosities are summarized in Table B.1. For each transition and box, we computed a correction factor, defined as the ratio of the luminosity from the fit to the luminosity from the spectrum, to account for the absorption features when estimating the luminosity from FIFI-LS. For the [O I] 63.18 μm , it is expected that FIFI-LS line fluxes are underestimated in average by a factor of 1.76 ± 0.16 , respectively.

Appendix C: Far-IR line luminosities along the DR21 Main outflow

Figure C.1 shows the position and size of boxes used for the line luminosity calculation along the major axis of DR21 Main outflow in Section 4.1. The size of boxes was optimized to contain continuous emission on the maps of [O I], [O III], CO, and [C I], e.g., to take advantage of the entire extent of the outflow and to avoid the “holes” in the CO map. Noteworthy, the emission in [O III] is mostly present in the eastern outflow-lobe and not detected in several positions along the outflow.

Table C.1 shows the line luminosities of far-IR lines observed with FIFI-LS for each box. The offsets are calculated with respect to the coordinates of the DR21 Main center (Section 4).

Appendix D: UV radiation field estimates from the continuum maps

Figure D.1 shows the distribution of UV field strengths toward DR21 Main derived from the 70 and 160 μm maps from *Herschel*, following standard methods (Schneider et al. 2016, and references therein), assuming that the UV radiation from the central stars is fully absorbed and re-radiated by the dust at far-IR.

The 70 μm map was convolved to match the 160 μm resolution ($\sim 12''$), and subsequently both maps were resampled to a pixel size of $2''$. The intensities at 70 and 160 μm were obtained using the bandwidths of 20 and 75 μm , respectively. The intensity close to the Spectral Energy Distribution peak ($\sim 115 \mu\text{m}$) was estimated from the average intensities at 70 and 160 μm using the bandwidth of 45 μm . The UV field, in units of Habing, was calculated from the following scaling relation (see Schneider et al. 2016):

$$F_{UV} = \frac{4\pi I_{FIR}}{G_0} \quad (\text{D.1})$$

where I_{FIR} is the sum of the intensities between 70 and 160 μm , and the average interstellar radiation field, G_0 , equals 1.6×10^{-3} $\text{erg cm}^{-2} \text{s}^{-1}$ (Habing 1968; Kaufman et al. 1999). We obtained the UV field strengths of $\sim 10^5$ at the center of DR21 Main, which are consistent with the value of $\sim 2 \cdot 10^5$ (in Habing units) obtained from the modeling of far-IR lines (Ossenkopf et al. 2010). The UV fields drop to a few 10^2 - 10^3 at the outer edges of the outflow, including the interaction region (Fig. D.1). However, a contribution of cold dust to the 160 μm can be quite significant in the DR21 Main, and the derived UV fields should be considered as upper limits.

UV fields obtained from dust also agree with the amount of irradiation in the far-IR from the two O-type 6, two O-type 8, and two O-type 9 stars powering the central H II region of DR21 (Roelfsema et al. 1989), which we estimated as $\sim 1.4 \cdot 10^5$ at the edge of the H II region. Here, we followed the method described in Schneider et al. (2023) and used the stellar parameters from Martins et al. (2005). Due to the significant amount of dust associated with the DR21 ridge, we refrain from estimating the exact UV fields from stars at larger distances along the DR21 Main outflow.

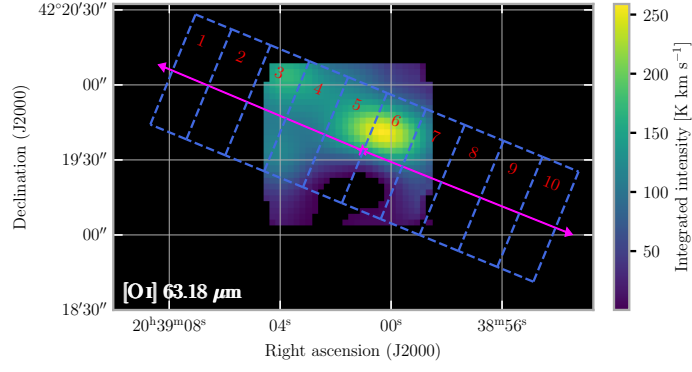


Fig. B.2: Integrated intensity map of the [O I] line at $63.18 \mu\text{m}$ from GREAT.

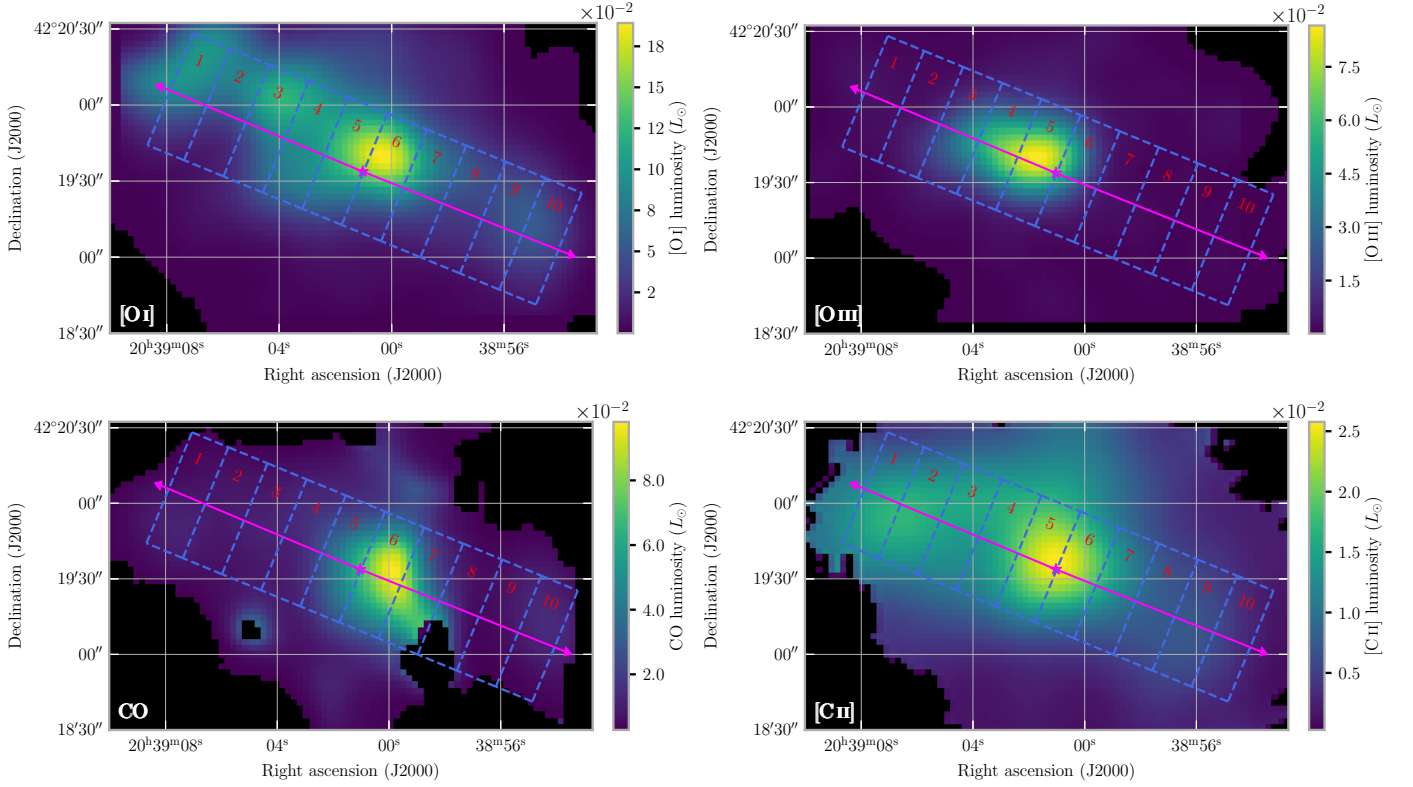


Fig. C.1: Luminosity maps of [O I] (top left), [O III] (top right), CO (bottom left) and [C II] (bottom right) shown at their native resolution.

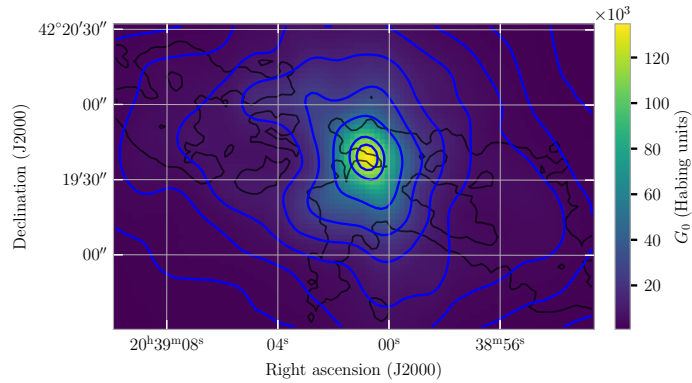


Fig. D.1: UV field strengths toward DR21 Main obtained from the *Herschel* dust continuum maps at 70 and $160 \mu\text{m}$. The blue contours correspond to G_0 of 10^3 , $1.8 \cdot 10^3$, $3.4 \cdot 10^3$, $6.5 \cdot 10^3$, $1.3 \cdot 10^4$, $2.5 \cdot 10^4$, $5 \cdot 10^4$, 10^5 , and $1.2 \cdot 10^5$ in Habing units. The gray contours in the background show the distribution of HCO^+ 1-0 from Skretas et al. (2023).

Table B.1: Comparison of luminosities of the [O I] line using FIFI-LS and GREAT

Box	$L_{[\text{O I}]63}$			
	FIFI-LS	GREAT	Fit to profile	Correction factor
3	8.09	9.20	13.90	1.51
4	9.57	20.34	34.95	1.72
5	10.08	22.95	44.72	1.95
6	10.28	21.11	37.91	1.80

Notes. The "Fit to profile" column refers to the total luminosities measured from the Gaussian fit to the line profiles unaffected by absorption, see Figure B.1. The correction factor is the ratio of the luminosity from the fit to that of the GREAT spectrum.

Table C.1: Line luminosities of far-IR species inside each box along the major axis of the DR21 Main outflow (Fig. C.1)

Box	Offset (")	$L_{\text{CO}14-13}$ (L_{\odot})	$L_{\text{CO}16-15}$ (L_{\odot})	$L_{[\text{O I}]63}$ (L_{\odot})	$L_{[\text{C II}]158}$ (L_{\odot})	$L_{[\text{O I}]145}$ (L_{\odot})	$L_{[\text{O III}]52}$ (L_{\odot})	$L_{[\text{O III}]88}$ (L_{\odot})	$L_{\text{OH}163}$ (L_{\odot})
1	75.3	0.18±0.04	0.15±0.03	8.64±1.73	1.87±0.37	0.84±0.17	0.22±0.04	0.22±0.04	0.01±0.01
2	58.5	0.16±0.03	0.12±0.02	6.39±1.28	2.09±0.42	1.02±0.20	0.37±0.07	0.47±0.09	0.01±0.01
3	41.7	0.18±0.04	0.18±0.04	10.27±2.05	2.02±0.40	1.05±0.21	1.69±0.34	1.26±0.25	0.04±0.01
4	24.9	0.27±0.05	0.32±0.06	11.93±2.39	2.20±0.44	1.28±0.26	3.23±0.65	2.28±0.46	0.08±0.02
5	8.1	0.71±0.14	0.66±0.13	13.39±2.68	2.84±0.57	1.94±0.39	3.69±0.74	3.03±0.61	0.12±0.02
6	-8.7	0.68±0.14	0.73±0.15	13.56±2.71	2.49±0.50	1.31±0.26	1.41±0.28	1.40±0.28	0.11±0.02
7	-25.5	0.28±0.06	0.34±0.07	7.49±1.50	1.51±0.30	0.56±0.11	0.17±0.03	0.28±0.06	0.04±0.01
8	-42.3	0.09±0.02	0.11±0.02	4.47±0.89	1.02±0.20	0.31±0.06	0.11±0.02	0.13±0.03	0.01±0.01
9	-59.1	0.21±0.04	0.16±0.03	4.76±0.95	0.90±0.18	0.32±0.06	0.09±0.02	0.08±0.02	0.04±0.01
10	-75.9	0.27±0.05	0.19±0.04	4.27±0.85	0.55±0.11	0.23±0.05	0.10±0.02	0.05±0.01	0.03±0.01